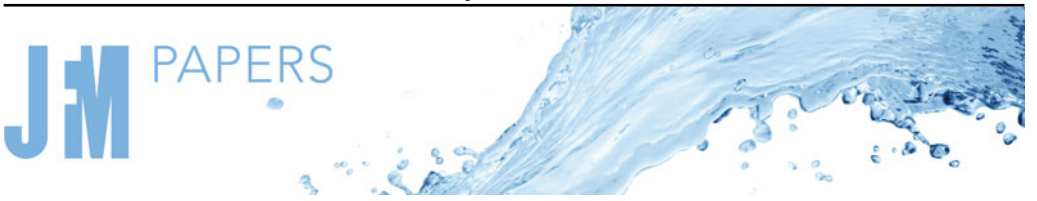
J. Fluid Mech. (2026), *vol.* 1032, A27, doi:10.1017/jfm.2026.11382



A triple source model of pressure fluctuation analysis for a mixed-flow pump

Bingfu Han[1] **and Lei Tan**[1]

[1]State Key Laboratory of Hydroscience and Engineering, Department of Energy and Power Engineering, Tsinghua University, Beijing 100084, PR China

Corresponding author: Lei Tan, tanlei@mail.tsinghua.edu.cn

(Received 9 October 2025; revised 29 January 2026; accepted 3 March 2026)

This paper investigates the physical origins of pressure fluctuations on the stationary shroud wall of a mixed-flow pump. A novel 'triple source model' is developed and applied to experimental validated stress-blended eddy simulations. The model decomposes stationary-frame pressure fluctuations into three distinct rotating-frame components to disentangle complex tip leakage vortex (TLV) interactions: (i) kinematic 'non-uniform fluctuation' (p_{NUF}) from the steady blade sweep, (ii) dynamic 'flow synchronous fluctuation' (p_{FSF}) phase-locked to rotation, and (iii) 'flow asynchronous fluctuation' (p_{FAF}) from all non-phase-locked phenomena. Analysis reveals that shroud unsteadiness is over 90 % dominated by the synchronous components along the TLV trajectory. Crucially, the model uncovers a counter-intuitive destructive interference mechanism between the kinematic sweep p_{NUF} and the dynamic response p_{FSF}, with local cross-correlation coefficient –0.26, explaining how dynamic instabilities can dampen the steady pressure footprint. Source-term analysis of the pressure Poisson equation establishes a complete causal chain from specific velocity field interactions to pressure signatures: (i) the non-uniform fluctuation is kinematically driven by the mean momentum flux from blade loading, contributing 52.27 % to the local pressure asymmetry; (ii) the flow synchronous fluctuation is generated by periodic vortex–turbulence interaction, contributing 80.22 % of its total source; (iii) and the asynchronous broadband pressure is sourced from the canonical turbulent cascade, contributing 79.33 % of its total source. Spatial correlations confirm the TLV as the common physical nexus for all components. This work establishes a quantitative diagnostic framework that moves beyond qualitative vortex observation, providing a physical basis for the targeted mitigation of turbomachinery unsteadiness.

Key words: rotating turbulence, vortex dynamics, hydrodynamic noise

© The Author(s), 2026. Published by Cambridge University Press.

https://doi.org/10.1017/jfm.2026.11382 Published online by Cambridge University Press

1. Introduction

Pressure fluctuations are a defining feature of the flow in turbomachinery, where high Reynolds number turbulence, complex vortex dynamics and rotor–stator interactions generate an intensely unsteady pressure field (Zuo *et al.* 2015). The unsteady pressure field acting on wall surfaces induces high-frequency structural vibrations, generates significant hydro-acoustic and aero-acoustic noise, and can ultimately lead to material fatigue and failure (Keller, Kumar & Mahesh 2018; Lv *et al.* 2024). A fundamental understanding of the underlying physical sources of these fluctuations is therefore essential for the development of effective flow control and noise mitigation strategies, as well as for the design and safe operation of modern turbomachinery.

For a stationary observer, such as a pressure transducer mounted on the shroud wall, the measured pressure signal can be attributed to two distinct sources: (i) a kinematic contribution tied to the relative motion of frames of reference, and (ii) a dynamic contribution stemming from genuine temporal variations in the flow field.

The kinematic contribution arises when a stationary probe samples a pressure field that, while steady in the rotating frame of reference, is spatially non-uniform. As the rotor blades, with their associated high-pressure and low-pressure regions, sweep past a fixed sensor, this spatial pressure distribution is recorded as a temporal fluctuation. This concept was first formalised by Kemp & Sears (1953), who identified this 'potential flow interaction' as a primary source of unsteadiness, explicitly distinguishing it from the interaction caused by viscous wakes. For the purpose of analytical modelling, Kingan & Parry (2019) decomposed the unsteady flow field generated by each propeller blade into (i) the viscous wake, (ii) the tip vortex, and (iii) the bound potential field, further demonstrating the significant role of the kinematic effect of this potential field in the unsteady flows of rotating machinery. The importance of rigorously modelling this effect is particularly evident in various theoretical and computational frameworks. To account for this key component of interaction noise, researchers have developed corresponding analytical source models, such as that by Parry & Crighton (1989) for the attached potential field. This principle can be directly extended to computational frameworks. For instance, the linearised Euler equations (Hall & Clark 1991) are based on decomposing the flow into a steady base flow and a small, harmonic unsteady perturbation. Within this framework, the steady flow field in the moving reference frame appears as a variable coefficient, thereby intrinsically and systematically capturing this quasi-steady (or kinematic) effect. This kinematic source is inherently deterministic and periodic, manifesting primarily as discrete tones at the blade passing frequency (BPF) and its harmonics, as described by the classic acoustic mode theory of Tyler & Sofrin (1962), and often dominating the pressure spectrum (Liang *et al.* 2024; Zhang *et al.* 2025).

In contrast, the dynamic contribution originates from inherent instabilities and unsteady phenomena of the fluid itself, which are genuinely time-varying in any frame of reference. They can be broadly categorised as three parts.

(i) Deterministic (phase-locked). These dynamic events are synchronised with the rotor's period of rotation. A classic example is the viscous rotor–stator interaction, where viscous wakes shed from an upstream blade row periodically impinge on a downstream blade row, causing fluctuations in incidence, loading and pressure (Li *et al.* 2024; Wei *et al.* 2025). In shrouded machinery with tip clearance, another key source is the inherent unsteadiness of the tip leakage vortex (TLV). The TLV is far from a steady structure and is known to exhibit complex dynamics such as meandering, kinking and periodic breakdown, leading to significant pressure

https://doi.org/10.1017/jfm.2026.11382 Published online by Cambridge University Press

fluctuations on the blade suction side and the shroud wall (You *et al.* 2007; Liu & Tan 2018). These phase-locked dynamic events also contribute to the discrete tones at the BPF and its harmonics. In-depth analytical modelling by Roger, Schram & Moreau (2014) and Quaglia *et al.* (2017) has shown that accurately predicting the resulting unsteady blade loading and acoustic signatures requires considering the detailed three-dimensional structure of the vortices, including their axial velocity deficit. These studies underscore the necessity of clearly distinguishing the pressure signature produced by the genuine dynamic event from that of the background potential field.

(ii) Organised (non-synchronous unsteadiness). Such phenomena possess their own characteristic frequencies, independent of the rotor speed. The most typical examples are rotating stall – a disturbance involving one or more stall cells propagating at a fraction of the rotor speed (Kameier & Neise 1997; Widmer, Staubli & Ledergerber 2011) – and surge, an axisymmetric mass flow oscillation throughout the entire machine (Callenaere *et al.* 2001). These phenomena generate strong, low-frequency pressure pulsations that severely limit the operating range and threaten structural integrity.

(iii) Stochastic (broadband). This category includes all random, non-deterministic fluctuations, which primarily originate from turbulence. Turbulence is generated in blade boundary layers, shear layers and wakes. Its convection through the flow passage results in broadband pressure signatures, forming the 'floor' of the noise and vibration spectra (Shi, Tang & Huang 2022; Duan *et al.* 2024).

These three types of contributions are not entirely mutually exclusive; for instance, deterministic events such as vortex breakdown can simultaneously generate stochastic turbulence.

In the field of aero-acoustics, the challenge of separating these superimposed effects is particularly pronounced, as the goal is to predict far-field sound radiation. The extensive research on propeller noise by Kingan and Parry offers a highly relevant analogy to the problem addressed herein. They developed an asymptotic theory capable of identifying the precise locations on a blade – the 'critical points' – that dominate the generation of specific pure tones (Kingan & Parry 2019; Parry & Kingan 2019). Their analysis essentially distinguishes between the steady loading contribution (analogous to the kinematic source) and the wake interaction contribution (a type of dynamic source). They demonstrated that the relative phase between these sources, governed by factors such as blade sweep, determines whether the final acoustic radiation is amplified or attenuated (Kingan & Parry 2020*b*). Their 'event line' concept, whose precession speed is determined by the interaction mode (Parry & Kingan 2021), provides an intuitive temporal–spatial picture of the ordered structures resulting from the superposition of kinematic and dynamic effects. This distinction is far from a purely academic exercise; it is crucial for effective design and control. In aero-acoustics, blade sweep is designed precisely to de-phase the acoustic signals generated along the span, a goal achievable only with accurate models for each source type (Parry 1995; Kingan & Parry 2020*a*).

Similarly, in the hydrodynamics context of this paper, the triple decomposition – pioneered by Reynolds & Hussain (1972) and later adapted for turbomachinery analysis by Adamczyk (1999) – provides a robust framework for decomposing superimposed pressure fluctuations (Lignarolo *et al.* 2015). Virgilio *et al.* (2024) used a phase-locked triple decomposition to study the interaction between the tip vortex of a dual-propeller and the turbulent boundary layer on the hull, revealing how tip clearance modulates the amplitudes of both periodic and random fluctuations. Mao *et al.* (2024) applied triple decomposition

https://doi.org/10.1017/jfm.2026.11382 Published online by Cambridge University Press

in both stationary and rotating frames to analyse velocity and pressure fluctuations in a mixed-flow fan, detailing its unsteady flow features, and highlighting differences from aero-engine fan spectra. Building on this analysis, they later combined the technique with source identification methods to separate tonal and broadband noise sources (Mao *et al.* 2025). However, a direct application of the standard triple decomposition framework in a stationary frame lumps the purely kinematic sweeping effect together with all other phase-locked dynamic events into a single 'phase-averaged' component. This prevents one from isolating the pressure signature of genuine flow instabilities from the background signal created by the steady blade loading. This ambiguity severely impedes a fundamental understanding of the root causes of pressure fluctuations, and consequently hinders the development of effective control strategies.

It is important to note that while a single coherent structure, such as the TLV, is often the common physical origin governing the entire unsteady field, the mechanisms by which it generates pressure fluctuations perceived by a stationary observer vary fundamentally. The triple source model is designed not to sever this physical connection, but rather to disentangle the convoluted contributions arising from the mere existence of the vortex (kinematic) versus its intrinsic instability (dynamic). This distinction is vital for engineering control: whereas a direct flow analysis might suggest stabilising the vortex to reduce noise, the present model can determine whether the dominant source is the kinematic sweeping of the steady loading, which would instead require a modification of the blade geometry.

To resolve this fundamental ambiguity, this paper introduces a novel analytical framework – the 'triple source model' – which aims to explicitly separate the aforementioned convoluted contributions. By employing a transformation to systematically link the triple decomposition in the stationary frame to its counterpart in the rotating frame, this model rigorously partitions the total pressure fluctuation in the stationary frame into three physically distinct and interpretable components: (i) the kinematic 'non-uniform fluctuation' (p_{NUF}), which isolates the quasi-steady sweeping effect of the mean rotor pressure field, analogous to the classical 'potential flow interaction'; (ii) the dynamic 'flow synchronous fluctuation' (p_{FSF}), which represents genuine, phase-locked unsteady flow events originating within the rotor's frame of reference; and (iii) the 'flow asynchronous fluctuation' (p_{FAF}), which encompasses all non-phase-locked events, including turbulence. Furthermore, to establish a direct causal link from the flow dynamics to the observed pressure signatures, this decomposition is integrated with a source-term analysis of the pressure Poisson equation. This allows each of the three pressure components to be traced back to its root origins in the velocity field, thereby revealing the precise fluid dynamic mechanisms upon which each is generated.

This paper formally presents this 'triple source model' and applies it to a high-fidelity simulation of a mixed-flow pump, demonstrating its power in unambiguously revealing the physical origins of pressure fluctuations in turbomachinery. The remainder of this paper is organised as follows. Section 2 details the experimental set-up and the high-fidelity numerical methodology, including a rigorous validation against measurement data. Section 3 introduces the theoretical framework for the triple source model based on triple decomposition, and applies it to the simulation data to quantify the different physical sources. In § 4, a source-term analysis using the pressure Poisson equation is conducted to uncover the mechanistic origins of each fluctuation component. Finally, § 5 summarises the key findings and offers perspectives for future research.

https://doi.org/10.1017/jfm.2026.11382 Published online by Cambridge University Press

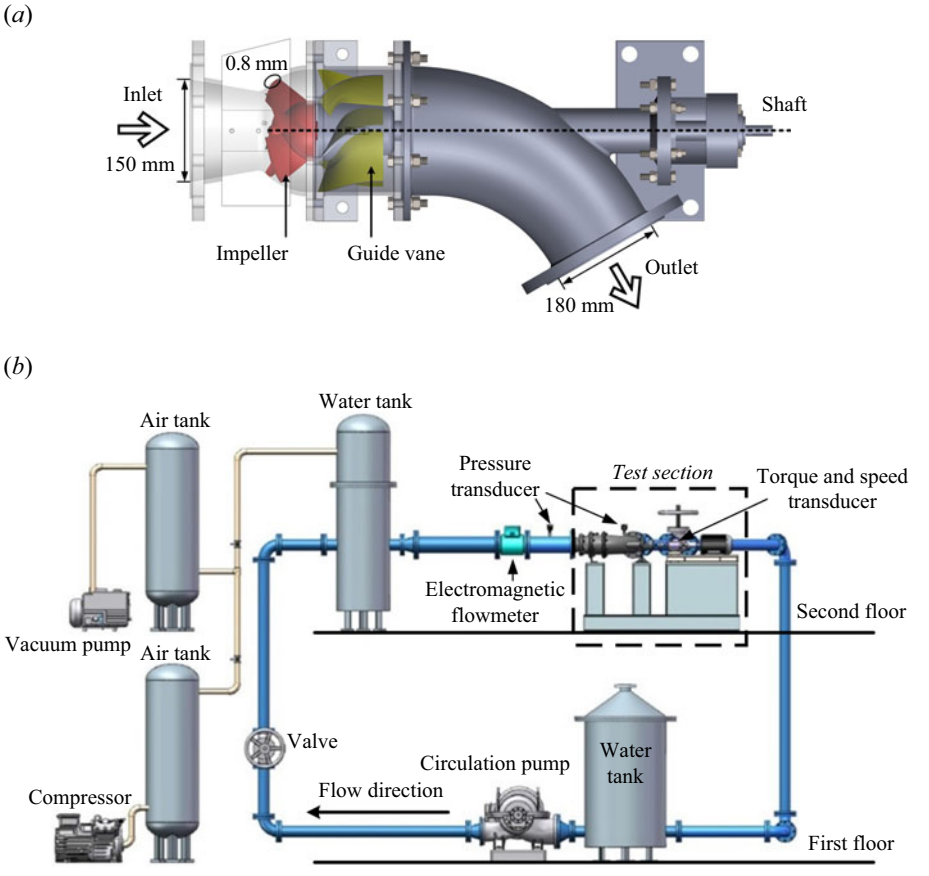


Figure 1. Experimental set-up: (*a*) the test mixed-flow pump; (*b*) the closed-loop hydraulic test rig.

2. The experimental and numerical dataset

2.1. *Experimental set-up*

The experiments were performed on a semi-open, five-bladed mixed-flow pump with a six-vaned diffuser, as illustrated in figure 1(*a*). It is designed for flow rate (Q_d) 0.0346 $m^3\ s^{-1}$ and head (H_d) 2.57 m at rotational speed (n_d) 1450 rpm. This corresponds to a BPF $f_{BPF} \approx 121$ Hz. Based on the impeller outlet diameter ($D_2 = 0.18$ m) and tip speed, the Reynolds number is $Re \approx 2.2 \times 10^6$, indicating a fully turbulent flow regime. For all experiments, the tip clearance was maintained at a constant 0.8 mm, corresponding to a non-dimensional clearance of 0.44 % of the impeller outlet diameter. This value not only is representative for the pump, but also allows the present analysis to build directly upon a well-characterised baseline case from the previous studies (Han & Tan 2023*a*,*b*; Han, Tan & Han 2024).

The pump was tested in a closed-loop hydraulic facility at Tsinghua University, as shown in figure 1(*b*), that has yielded previously published results (Lu *et al.* 2022; Han & Tan 2023*a*). The uncertainties of the primary measured variables are as follows: flow rate (Q) is ±0.2 %, torque (T) is ±0.2 %, rotational speed (n) is ±1 rpm (equivalent to ±0.069 % at the design point), and inlet/outlet pressures (p) are ±0.065 %. Based on these instrument accuracies, the maximum relative uncertainties for the head H, shaft power P, and pump efficiency η are estimated to be ±0.15 %, ±0.21 % and ±0.32 %, respectively.

https://doi.org/10.1017/jfm.2026.11382 Published online by Cambridge University Press

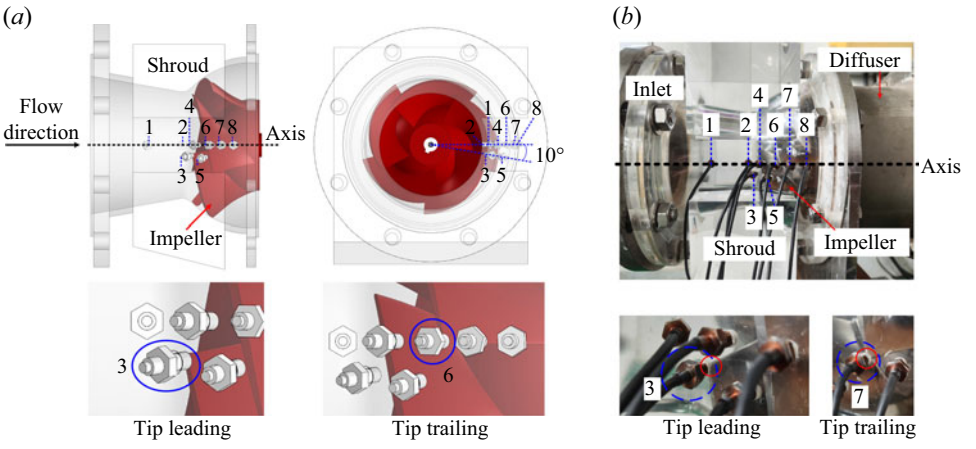


Figure 2. Arrangement of the eight high-frequency dynamic pressure sensors on the shroud wall, showing (*a*) the schematic model and (*b*) a photograph of the experimental set-up. The sensors are positioned at dimensionless axial locations $z^* = (z - z_l)/(z_t - z_l) = -2.38, -0.46, 0, 0.33, 0.67, 1, 1.54, 2.15$, corresponding to sensors 1–8, respectively. Sensor 3 aligns with the blade tip leading edge, and sensor 6 with the trailing edge. For installation purposes, sensors 3 and 5 are circumferentially offset by 10°.

The primary focus of this study, the unsteady pressure on the stationary shroud, was investigated using an array of eight flush-mounted, high-frequency pressure sensors (Model CYG515A, range 0–200 kPa (absolute), accuracy 0.25 %), as detailed in figure 2. Flush-mounting is critical to prevent artefacts from flow-induced sensor vibration or cavity resonance (Camussi *et al.* 2010). The sensors were installed in 5 mm diameter ports, each featuring a pressure tap with 0.7 mm diameter orifice and 1 mm depth. This small orifice size is crucial for minimising spatial-averaging effects, which can attenuate the signature of high-wavenumber turbulent structures (Hu 2022; Huang *et al.* 2024).

The sensors were arranged sequentially along the shroud to capture the axial development of the flow. Their positions are defined by the dimensionless axial coordinate $z^* = (z - z_l)/(z_t - z_l)$, where z is the axial position, and $z_l = 0.106$ m and $z_t = 0.128$ m are the axial positions of the blade tip leading edge and trailing edge, respectively. The dimensionless locations for sensors 1–8 are $-2.38, -0.46, 0, 0.33, 0.67, 1, 1.54, 2.15$. Notably, sensor 3 aligns with the leading edge, and sensor 6 with the trailing edge. This axial array is complemented by circumferential offset 10° for sensors 3 and 5 relative to the main sensor line. This strategic offset is dual-purpose: it enables the capture of azimuthal phase variations, essential for reconstructing spatio-temporal flow features (Kameier & Neise 1997), while also ensuring adequate physical spacing between ports to mitigate potential acoustic crosstalk or sensor-induced flow alterations.

Data were acquired synchronously using a 16-channel acquisition system at sampling frequency 5120 Hz, which is more than 40 times the BPF, and ensures resolution of at least the first 20 harmonics. This bandwidth is adequate for capturing the primary energy-containing frequencies associated with rotor–stator interaction, as demonstrated in similar pump configurations (Luo *et al.* 2024). At each measured operating conditions, signals were recorded for 15 s, equivalent to approximately 362.5 rotor revolutions, ensuring robust statistical convergence of phase-averaged quantities (Feng, Benra & Dohmen 2007). A notch filter was applied to the raw data to remove noise at the 50 Hz power line frequency and its harmonics. The total uncertainty for the unsteady pressure signal, accounting for the data acquisition system, is determined to be within ±0.82 %.

https://doi.org/10.1017/jfm.2026.11382 Published online by Cambridge University Press

2.2. *Numerical set-up*

The flow within the mixed-flow pump is simulated by solving the spatially filtered, incompressible Navier–Stokes equations. The governing equations for the resolved velocity field $\hat{u}_i(\boldsymbol{x}, t)$ and pressure field $\hat{p}(\boldsymbol{x}, t)$ are given by

$$\frac{\partial \hat{u}_i}{\partial x_i} = 0, \tag{2.1}$$

$$\frac{\partial \hat{u}_i}{\partial t} + \frac{\partial (\hat{u}_i \hat{u}_j)}{\partial x_j} = -\frac{1}{\rho}\frac{\partial \hat{p}}{\partial x_i} + \nu \nabla^2 \hat{u}_i - \frac{\partial \tau_{ij}}{\partial x_j}, \tag{2.2}$$

where $\hat{(\cdot)}$ denotes spatial filtering. The unclosed term $\tau_{ij} = \widehat{u_i u_j} - \hat{u}_i \hat{u}_j$ is the subgrid-scale stress tensor, representing the effect of unresolved turbulent scales.

The accurate resolution of multi-scale turbulent structures is paramount for this study. These structures encompass not only the fine-scale dynamics associated with the formation, development and subsequent breakdown of the TLV, but also the large-scale coherent motions originating from the unsteady rotor–stator interaction. To address these phenomena with a high degree of fidelity yet within a computationally feasible framework, the stress-blended eddy simulation (SBES) model (Menter & Egorov 2010), as implemented in ANSYS CFX, was adopted for all simulations.

The foundation of the SBES model is the shear-stress transport (SST) $k-\omega$ model (Menter 1994). The SST model is widely recognised for its robust performance in flows with attached boundary layers and moderate separation. It blends the $k-\omega$ model in the near-wall region with the $k-\varepsilon$ model in the freestream and wake regions. The transport equations for the turbulent kinetic energy k and the specific dissipation rate ω are

$$\frac{\partial (\rho k)}{\partial t} + \frac{\partial (\rho u_j k)}{\partial x_j} = P_k - \beta^* \rho \omega k + \frac{\partial}{\partial x_j}\left[(\mu + \sigma_k \mu_t)\frac{\partial k}{\partial x_j}\right], \tag{2.3}$$

$$\frac{\partial (\rho \omega)}{\partial t} + \frac{\partial (\rho u_j \omega)}{\partial x_j} = \frac{\alpha}{\nu_t} P_k - \beta \rho \omega^2 + \frac{\partial}{\partial x_j}\left[(\mu + \sigma_\omega \mu_t)\frac{\partial \omega}{\partial x_j}\right] + 2(1 - F_1)\frac{\rho \sigma_{\omega 2}}{\omega}\frac{\partial k}{\partial x_j}\frac{\partial \omega}{\partial x_j}, \tag{2.4}$$

where P_k is the production term of turbulent kinetic energy, and μ_t is the turbulent eddy viscosity. All model coefficients and the blending function F_1 are as defined by Menter (1994).

The core concept of SBES is the direct blending of the Reynolds stress tensors. The total turbulent stress tensor τ_{ij}^{SBES} is a weighted combination of the SST and large eddy simulations (LES) components via a shielding function f_s:

$$\tau_{ij}^{SBES} = f_s \tau_{ij}^{SST} + (1 - f_s)\tau_{ij}^{LES}. \tag{2.5}$$

Here, τ_{ij}^{SST} is computed by the SST $k-\omega$ model, and τ_{ij}^{LES} is the subgrid-scale (SGS) stress from LES. The shielding function f_s is designed to protect the boundary layer, ensuring that it remains fully in SST mode, with $f_s = 1$ near the wall, and smoothly transitioning to $f_s = 0$ in the core flow.

To facilitate the transition from SST to LES, SBES introduces an additional sink term ε_{SBES} into the SST k-equation to mimic the energy dissipation at subgrid scales:

$$\varepsilon_{SBES} = \beta^* \rho \omega k \times f_{SBES}, \tag{2.6}$$

where the blending function f_{SBES} is defined as

$$f_{SBES} = \max\left[\frac{L_t}{C_{SBES}\Delta_{SBES}}(1 - f_s), 1\right] - 1. \tag{2.7}$$

https://doi.org/10.1017/jfm.2026.11382 Published online by Cambridge University Press

Item	Mesh 1	Mesh 2	Mesh 3	Mesh 4
Elements number ($\times 10^4$)	392.94	491.18	601.91	752.38
Head H_d (m)	2.01	2.05	2.09	2.10
Efficiency η (%)	74.91	75.56	76.00	76.13

Table 1. Grid independence study results for the mixed-flow pump at the design point.

Here, $L_t = \sqrt{k}/(\beta^*\omega)$ is the turbulent length scale, C_{SBES} is a model constant, and Δ_{SBES} is the local grid scale. This formulation ensures that the dissipative term is activated in regions where the grid resolution is fine enough to resolve turbulent eddies, thus enabling a seamless transition to LES mode.

The computational domain (figure 3*a*) includes the impeller, diffuser and extended inlet/outlet pipes. The outlet is simplified as a straight pipe. The locations of pressure monitoring points are set to be identical to the experimental positions. To ensure high-fidelity resolution of the multi-scale turbulent structures, a structured O-grid topology is employed in the near-wall and tip clearance regions. The numerical integrity of the simulation was established through a grid independence study using four sets of meshes. As shown in table 1, the predicted head and efficiency exhibited clear asymptotic behaviour as the mesh was refined. The discrepancy between meshes 3 and 4 is less than 0.5 % for head and 0.2 % for efficiency. Consequently, mesh 3, consisting of approximately 6.02×10^6 elements, was selected to balance computational cost with the required spatial resolution.

For this selected mesh, the height of the first grid layer was strictly controlled to maintain non-dimensional wall distance $y^+ < 1$ (figure 3*b*). This ensures that the SST component of the SBES model accurately resolves the viscous sublayer, providing a reliable wall boundary condition for the LES regions (Li *et al.* 2023). Crucially, the fidelity of this numerical set-up in capturing key flow features is demonstrated in figure 3(*c*). The simulation effectively resolves the complex three-dimensional topology. The spatial distribution of the SBES shielding function (f_s) is examined in figure 3(*d*). The results confirm that the entire tip clearance region and the trajectory of the TLV are located within the LES-active zone ($f_s = 0$), where multi-scale turbulent structures are directly resolved rather than modelled. The Reynolds-averaged Navier–Stokes (RANS) mode ($f_s = 1$) is appropriately restricted to the thin near-wall boundary layers.

A hybrid scheme combining a second-order central difference scheme with a first-order upwind scheme is employed for the advection term. A second-order backward Euler scheme is used for the transient term. The time step is set to $\Delta t = 2.29885 \times 10^{-4}$ s, which corresponds to a 2° rotation of the impeller per step. This temporal resolution yields sampling frequency approximately 4350 Hz, which is more than 35 times the BPF ($f_{BPF} \approx 121$ Hz). To ensure temporal independence of the numerical results, a sensitivity study was conducted using three different time steps corresponding to 1°, 2° and 4° of impeller rotation per step. The amplitudes and phases of f_{BPF} and its primary harmonics were compared at the shroud monitoring points. While the 4° time step exhibited noticeable discrepancies in capturing higher-order harmonics, the results for 2° and 1° showed excellent agreement, with the difference in BPF amplitude being less than 1.2 %. This asymptotic convergence confirms that the 2° time step adopted in this study is sufficient to accurately resolve the deterministic features while maintaining computational efficiency. A maximum of 20 inner iterations per time step are performed to ensure convergence. The convergence criteria are set as root mean square (RMS) less

https://doi.org/10.1017/jfm.2026.11382 Published online by Cambridge University Press

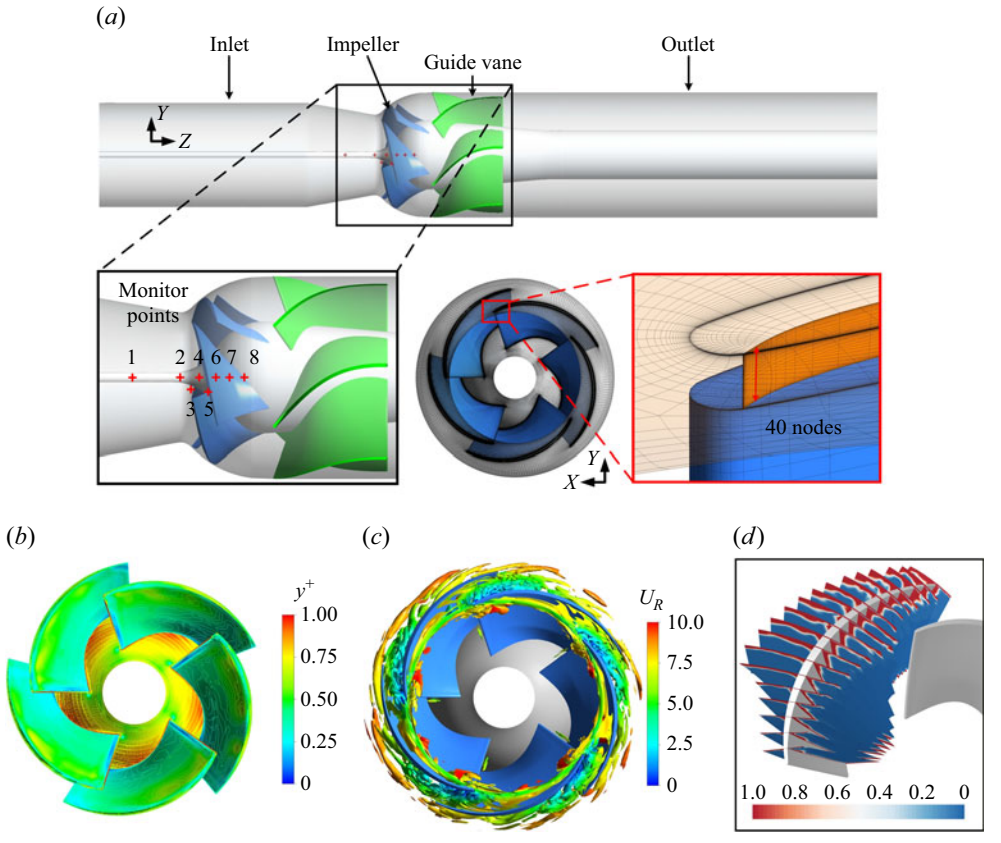


Figure 3. Schematic of the computational domain and numerical fidelity verification. (*a*) Overall view of the computational domain with mesh details. (*b*) Distribution of y^+ on blade and hub surfaces. (*c*) Vortex structures visualised by Q-criterion ($Q_{iso} = 10^6$), coloured by time-averaged relative velocity. (*d*) Distribution of the SBES shielding function f_s on multiple planes, where $f_s = 0$ (blue) denotes the LES region, and $f_s = 1$ (red) denotes the RANS region.

than 10^{-6}. The inlet boundary condition is specified as total pressure, while a mass flow rate is set at the outlet. A no-slip condition is applied to all solid walls.

2.3. *Data validation*

The accuracy of the SBES data is rigorously assessed by comparison with the experimental data, to establish the model's fidelity in capturing the key fluid-dynamic phenomena that underpin the pressure fluctuations investigated in this paper.

First, the model's ability to reproduce the time-averaged flow field and overall energy transfer is confirmed by comparing the predicted pump performance with experimental measurements over a wide range of flow rates. As shown in figure 4, the predicted head and efficiency curves are in excellent agreement with the experimental data. At the design point ($Q_d = 0.0346$ m^3 s^{-1}), the predicted head is $H_{SBES} = 1.94$ m and the efficiency is $\eta_{SBES} = 73.2$ %, corresponding to relative deviations of 2.7 % and 0.4 % from the experimental values, respectively. And the maximum discrepancies below 7 % across the entire operating range from partial load ($0.6Q_d$) to overload ($1.2Q_d$). This validates the simulation's representation of the mean hydrodynamics.

https://doi.org/10.1017/jfm.2026.11382 Published online by Cambridge University Press

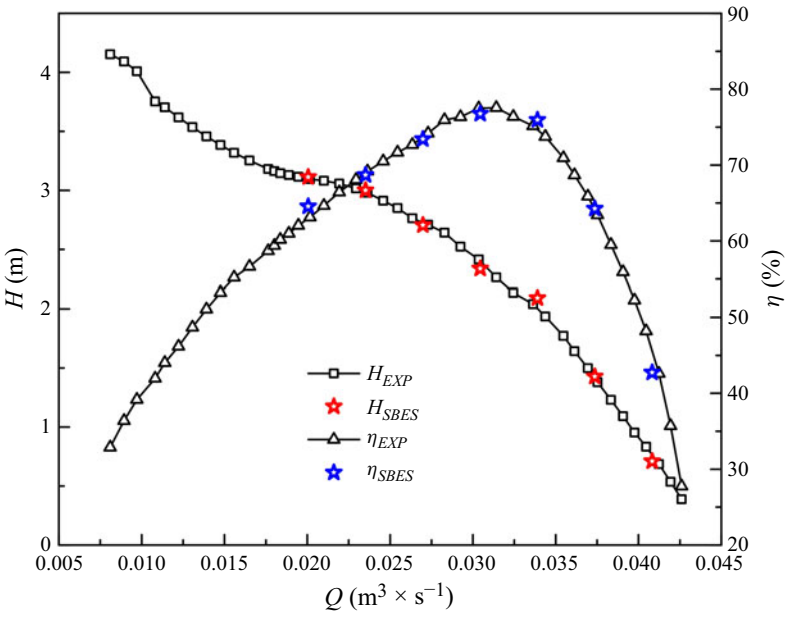


Figure 4. Global performance characteristics of the mixed-flow pump. The head (H) and efficiency (η) are plotted against the flow rate (Q). Experimental measurements (lines) are compared with numerical predictions from the SBES model at seven operating points (stars).

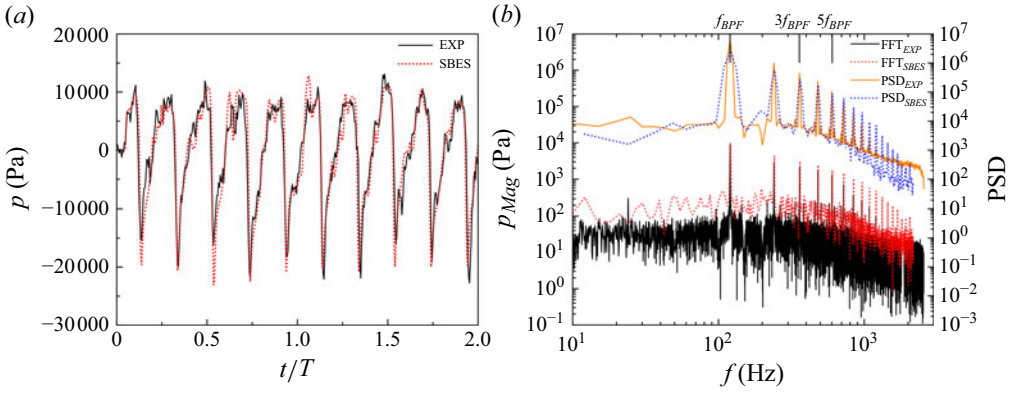


Figure 5. Time-domain pressure fluctuations (p') on the shroud wall at $0.8Q_d$. A comparison between experimental (EXP) and numerical (SBES) signals over two rotor revolutions (T) is shown for two axial locations: (a) monitoring point 4 ($(z - z_l)/(z_t - z_l) = 0.33$) and ($b$) monitoring point 5 ($(z - z_l)/(z_t - z_l) = 0.67$). Here, p_{Mag} denotes the pressure magnitude, FFT stands for Fast Fourier Transform, and PSD stands for Power Spectral Density.

A more critical validation is performed on the local unsteady pressure field at a representative partial load condition of $0.8Q_d$, where unsteady effects associated with the tip clearance flow are often more pronounced (Sun & Tan 2020; Yang *et al.* 2021). A comparison of the time-domain signals in figure 5(a) reveals a strong correspondence between the numerical and experimental waveforms at a representative location (point 5 with $z^* = 0.67$). This is quantitatively confirmed by the high cross-correlation coefficients between the phase-aligned signals ($R_{xy} = 0.93$), indicating that the simulation accurately

https://doi.org/10.1017/jfm.2026.11382 Published online by Cambridge University Press

reproduces the temporal structure and phase of the blade-induced pressure pulses. At point 5, the RMS value of the SBES fluctuating pressure is 8.29 kPa, which is within 4.1 % of the experimental measurement 8.63 kPa.

The spectral content of the signal, shown in figure 5(*b*), provides deeper insight into the model's performance. The simulation demonstrates high fidelity in capturing the discrete-tone frequency components, with the amplitudes of f_{BPF} and its primary harmonics being in excellent agreement with the experimental data. This success underscores the model's ability to resolve the dominant, deterministic sources of unsteadiness.

However, a discrepancy emerges in the broadband portion of the spectrum, particularly at higher frequencies ($f > 1000$ Hz), where the simulation under-predicts the energy content. This behaviour is a known limitation of hybrid RANS–LES approaches (Fröhlich & Von Terzi 2008). This under-prediction is primarily attributed to the time scale and length scale separation, where the grid filter and time step act as a low-pass filter, and the higher eddy viscosity in RANS-shielded regions provides excessive numerical damping. Furthermore, the simulation faces the 'grey area' challenge at the interface where the model transitions from RANS to LES. In this region, resolved turbulence requires a certain spatial and temporal development length to build up through nonlinear interactions, leading to a spectral deficit at high frequencies. Nevertheless, spectral analysis (figure 5*b*) confirms that over 90 % of the pressure fluctuation energy is concentrated in the BPF and its first few harmonics; the high-frequency broadband deficit does not undermine the primary conclusions or the identified interference mechanisms of this study.

In summary, this experimentally validated SBES dataset thus provides a robust and reliable basis for the triple source model decomposition in § 3 and the source-term analysis in § 4. For these forthcoming analyses, the time-averaged results are obtained by statistically averaging over 1800 instantaneous time steps, while the phase-averaged results are derived from an ensemble of 50 rotor passages.

3. Triple source model

3.1. *Theoretical framework*

The analysis of pressure fluctuations in turbomachinery faces a fundamental physical ambiguity: a stationary observer (such as a transducer mounted on the shroud) cannot inherently distinguish between fluctuations caused by the steady spatial non-uniformity of the rotor sweeping past, and those caused by genuine temporal flow instabilities. Standard analysis methods often conflate these two distinct mechanisms, obscuring the true physical origins of the unsteadiness. To resolve this 'observer's dilemma', this work introduces the triple source model. This framework establishes a physical mapping that projects the stationary-frame signals back to their distinct origins in the rotating frame of reference, thereby disentangling the kinematic effects of blade loading from the dynamic effects of flow instability.

Conventionally, an instantaneous pressure signal in the stationary frame, $P_S(\theta, z, t)$, is decomposed using the standard triple decomposition (Reynolds & Hussain 1972)

$$P_S(\theta, z, t) = \overline{P}_S(\theta, z) + \tilde{p}_S(\theta, z, t) + p'_S(\theta, z, t), \tag{3.1}$$

where $\overline{P}_S$ is the time-averaged mean, $\tilde{p}_S$ is the phase-locked (synchronous) fluctuation, and p'_S is the non-phase-locked (asynchronous) fluctuation. While mathematically valid, this decomposition is physically insufficient for identifying root causes. The synchronous component $\tilde{p}_S$ lumps together two fundamentally different phenomena.

https://doi.org/10.1017/jfm.2026.11382 Published online by Cambridge University Press

(i) The kinematic sweeping effect, arising from the pressure field attached to the blades (e.g. steady blade loading). This field is invariant in time within the rotating frame, but generates a periodic signal when sampled by a stationary probe.
(ii) The dynamic flow instability, arising from genuine time-dependent flow evolutions (e.g. the breathing or oscillation of the TLV) that are phase-locked to the rotation.

Without separating these, it is impossible to determine whether high-amplitude fluctuations are merely a kinematic artefact of high blade loading or a symptom of unstable vortex dynamics.

To isolate these mechanisms, the fluctuations must be traced to their origins in the rotating frame. An analogous decomposition is applied to the instantaneous pressure $P_R(\theta', z, t)$ in the rotating frame:

$$P_R(\theta', z, t) = \overline{P}_R(\theta', z) + \tilde{p}_R(\theta', z, t) + p'_R(\theta', z, t), \tag{3.2}$$

where θ' denotes the relative azimuthal coordinate. Here, $\overline{P}_R$ is the time-averaged steady pressure field of the rotor, and $\tilde{p}_R$ represents the deterministic, synchronous fluctuations observed on the rotating components.

The link between the two frames is established by the coordinate transformation $P_S(\theta, z, t) = P_R(\theta' = \theta - \Omega t, z, t)$, where Ω is the rotor angular velocity. By substituting the rotating-frame decomposition (3.2) into this transformation and applying the phase-average operator $\langle\cdot\rangle_S$ in the stationary frame, the components of the stationary signal can be rigorously derived. Recognising that the phase average of the asynchronous term is zero, and that the stationary time average $\overline{P}_S$ is equivalent to the azimuthal average of the rotating mean field $\langle\overline{P}_R\rangle_\theta$, the total Reynolds pressure fluctuation in the stationary frame can be expressed as a superposition of three physically distinct source terms:

$$p_S(\theta, z, t) = \underbrace{\left[\overline{P}_R(\theta', z) - \langle\overline{P}_R(\theta', z)\rangle_\theta\right]}_{p_{NUF}} + \underbrace{\tilde{p}_R(\theta', z, t)}_{p_{FSF}} + \underbrace{p'_R(\theta', z, t)}_{p_{FAF}}. \tag{3.3}$$

Equation (3.3) forms the core of the triple source model. Unlike the standard decomposition, each term on the right-hand side corresponds to a specific fluid-dynamic mechanism defined in the rotating frame.

(i) Non-uniform fluctuation (p_{NUF}): the kinematic source

$$p_{NUF}(\theta, z, t) = \overline{P}_R(\theta', z) - \langle\overline{P}_R(\theta', z)\rangle_\theta. \tag{3.4}$$

This term represents the purely kinematic signature of the steady blade loading. It originates from the time-averaged pressure field $\overline{P}_R$ in the rotating frame, which is structurally stable but spatially asymmetric. Physically, this corresponds to the classical 'potential flow interaction' (Kemp & Sears 1953). It is not a flow instability; rather, it is the work done by the steady pressure field of the rotor as it sweeps through the fluid volume.

(ii) Flow synchronous fluctuation (p_{FSF}): the dynamic source

$$p_{FSF}(\theta, z, t) = \tilde{p}_R(\theta', z, t). \tag{3.5}$$

This term captures the genuine deterministic instability of the flow. It corresponds to the phase-locked unsteadiness $\tilde{p}_R$ observed in the rotating frame. Physically, this represents coherent flow structures – such as the periodic expansion/contraction of the TLV or wake shedding – that evolve in time synchronously with the rotor passage. Unlike p_{NUF}, this term exists only when the flow field itself is time-dependent in the Lagrangian frame.

https://doi.org/10.1017/jfm.2026.11382 Published online by Cambridge University Press

(iii) Flow asynchronous fluctuation (p_{FAF}): the stochastic source

$$p_{FAF}(\theta, z, t) = p'_R(\theta', z, t). \tag{3.6}$$

This term encompasses all fluctuations not phase-locked to the rotor's rotation. It is dominated by random turbulence but can also include organised events (e.g. rotating stall) with intrinsic frequencies distinct from the shaft harmonics.

In summary, (3.3)–(3.6) provide the theoretical foundation for the remainder of this work. The principal advantage of this framework is the explicit isolation of the dominant kinematic sweep (p_{NUF}) from the underlying dynamic instabilities (p_{FSF} and p_{FAF}). This separation is crucial for diagnosing the true root causes of turbomachinery unsteadiness, as it prevents the misinterpretation of steady loading effects as flow instabilities.

3.2. *Triple sources of shroud wall pressure fluctuation*

3.2.1. *Dominance of synchronous and kinematic components*

To identify the primary drivers of shroud pressure unsteadiness, the triple source model is applied to the high-fidelity simulation data. Analysis at a representative monitoring point (point 5, situated within the high-unsteadiness region) reveals that the fluctuations are overwhelmingly deterministic and phase-locked to the rotor. As shown in the time-domain decomposition (figure 6), the synchronous component captures the primary periodic signature, accounting for 93.9 % of the total fluctuation energy.

The frequency-domain analysis (figure 7) confirms that the synchronous component contains all tonal energy at the BPF and its harmonics, while the asynchronous component forms the broadband floor. This dominance is not local; the spatial map of the RMS fluctuations (figure 8) highlights a 'hotspot' region over the impeller blade tip where the synchronous energy fraction consistently exceeds 90 % (figure 8*d*).

Crucially, the three source model reveals that these powerful tonal peaks are almost entirely attributable to the kinematic non-uniform fluctuation (p_{NUF}), whereas the flow synchronous fluctuation (p_{FSF}) – representing true dynamic instabilities – is substantially smaller (figure 8*b*). This indicates that the perceived unsteadiness is primarily a kinematic artefact of the stationary observer sweeping through the rotor's steady, non-uniform potential field. This phenomenon represents the hydrodynamic analogue of the classic 'potential flow interaction' (Kemp & Sears 1953) and aligns with the acoustic mode theory of (Tyler & Sofrin 1962). While standard triple decompositions isolate the tonal content, the three source model uniquely disentangles its kinematic and dynamic origins, pinpointing the steady blade loading as the root cause of the dominant pressure signature.

3.2.2. *The mechanism of destructive interference*

The finding that the kinematic p_{NUF} dictates the synchronous signal's character raises a subtle paradox. A closer inspection of the time-domain signals (figure 6*c*) and their respective variances reveals that the amplitude of p_{NUF} is, in fact, significantly larger than the total synchronous signal ($\tilde{p}_S$) that it helps create. This seemingly contradictory result points towards a crucial physical mechanism governing the final pressure signature: destructive interference between the kinematic and dynamic components.

The energetic relationship between the components is governed by the variance equation

$$\mathrm{Var}(\tilde{p}_s) = \mathrm{Var}(p_{NUF}) + \mathrm{Var}(p_{FSF}) + 2\, C_{NUF,FSF}\sqrt{\mathrm{Var}(p_{NUF})\,\mathrm{Var}(p_{FSF})}. \tag{3.7}$$

For the total variance $\mathrm{Var}(\tilde{p}_S)$ to be smaller than that of its largest constituent $\mathrm{Var}(p_{NUF})$, the covariance term, and thus the correlation coefficient $C_{NUF,FSF}$, must

https://doi.org/10.1017/jfm.2026.11382 Published online by Cambridge University Press

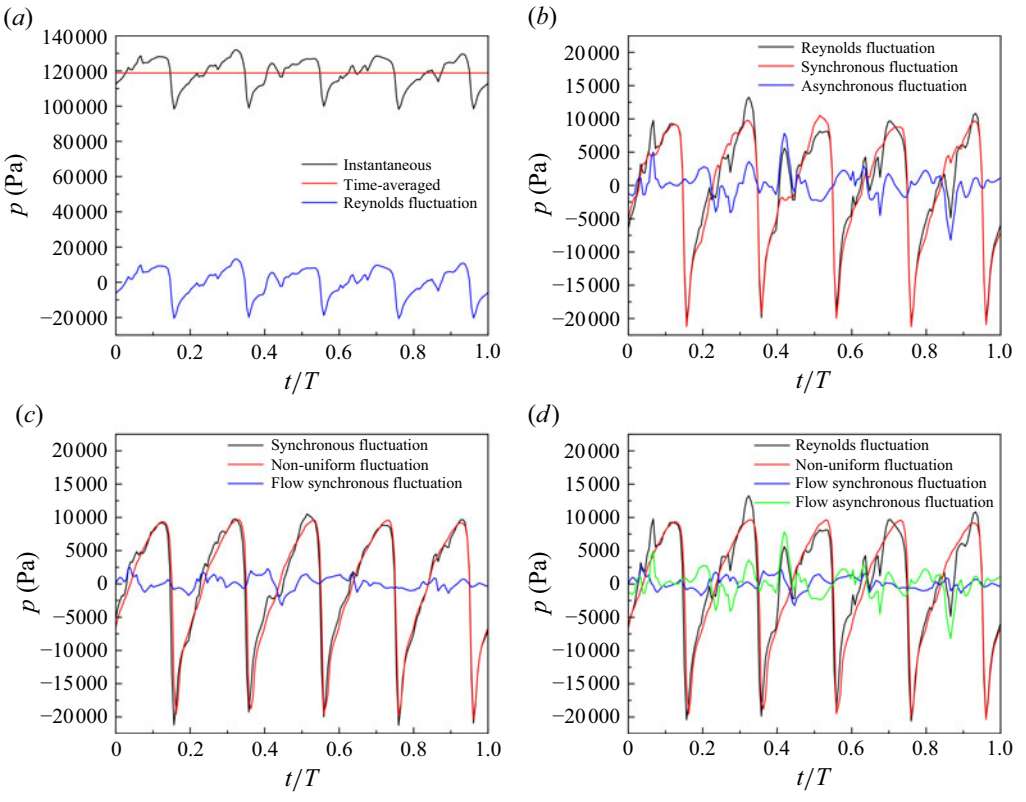


Figure 6. Time-domain decomposition of the pressure signal at monitoring point 5 ($0.8Q_d$). (*a*) Instantaneous signal and total Reynolds fluctuation. (*b*) Partitioning into synchronous and asynchronous (p_{FAF}) components. (*c*) Further decomposition of the synchronous signal into kinematic (p_{NUF}) and dynamic (p_{FSF}) sources. (*d*) Complete triple source decomposition.

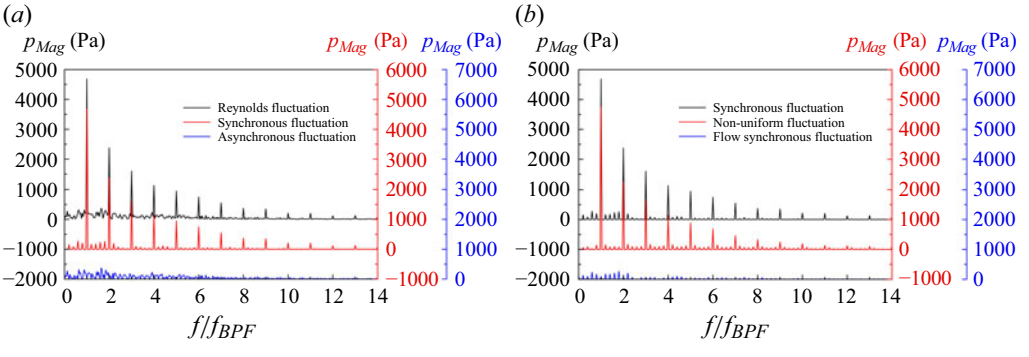


Figure 7. Frequency-domain analysis of the decomposed pressure components. (*a*) Separation of tonal peaks from the broadband floor. (*b*) Deconstruction of the synchronous spectrum, showing the dominance of kinematic p_{NUF} over dynamic p_{FSF}.

be negative. A direct calculation from the decomposed time series at point 5 confirms this, yielding $C_{NUF,FSF} = -0.26$. This negative correlation provides definitive quantitative proof of a predominantly anti-phase relationship between the kinematic sweep and the dynamic flow response at this location.

https://doi.org/10.1017/jfm.2026.11382 Published online by Cambridge University Press

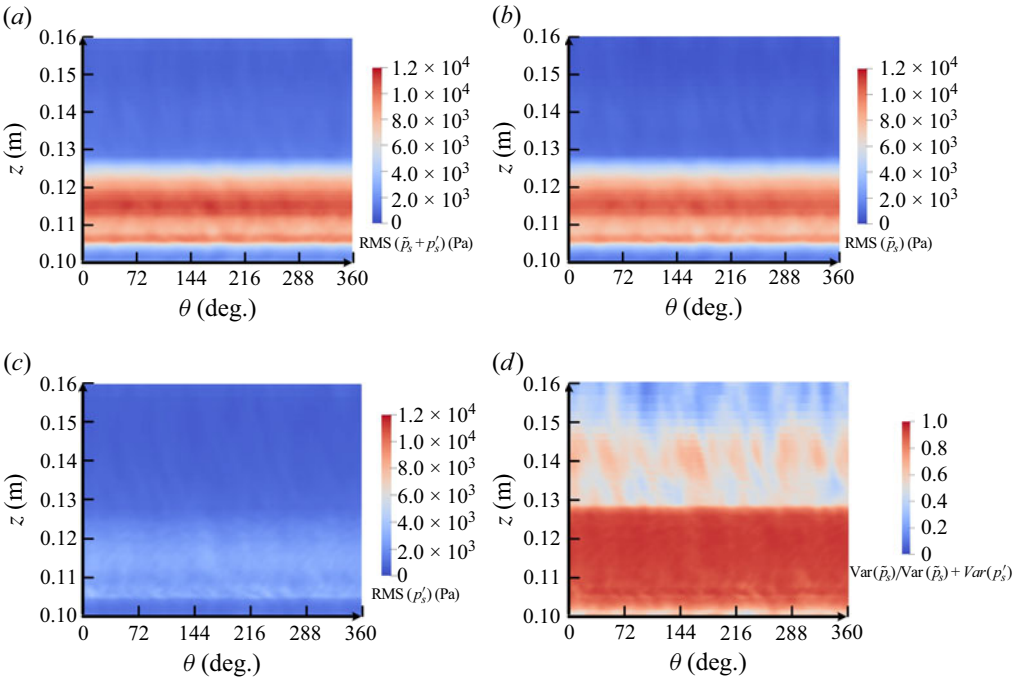


Figure 8. Spatial distribution of the decomposed components in the stationary frame. (*a*) Total Reynolds fluctuation RMS. (*b*) Synchronous fluctuation RMS. (*c*) Asynchronous fluctuation RMS. (*d*) Synchronous energy fraction.

Crucially, this discovery of destructive interference provides a critical physical insight that cannot be obtained through a direct analysis of coherent flow structures alone. A straightforward analysis of the TLV topology might suggest that a stronger vortex leads to higher pressure fluctuations; however, the present model reveals a counter-intuitive phenomenon where the dynamic instability effectively dampens the kinematic impact. At the blade tip, the dynamic oscillation of the vortex (p_{FSF}) is found to be largely out of phase with the deep pressure trough of the mean vortex field (p_{NUF}). Without this explicit decomposition, this cancellation mechanism would remain invisible, as a direct analysis would only show the final resultant pressure. This insight provides a new strategy for noise reduction through phase engineering, potentially allowing designers to amplify this interference to attenuate the final acoustic radiation.

Figure 9 offers a direct visualisation of this interference mechanism within a single blade passage. The large-amplitude trough of the kinematic p_{NUF}, which represents the passage of the blade tip's low-pressure suction side, is systematically modulated by the dynamic p_{FSF}. Critically, at this location, a local peak in the p_{FSF} signal consistently aligns with the primary trough of p_{NUF}. This alignment results in a partial cancellation, thereby reducing the amplitude of the final synchronous signal. The perceived pressure fluctuation is therefore not a single physical event, but a delicate superposition of a powerful, quasi-steady kinematic sweep, and a subtler, opposing dynamic response.

This concept of interference between quasi-steady loading effects and unsteady dynamic phenomena is not unique to hydrodynamics and finds a strong parallel in the field of aero-acoustics. For instance, the work of Kingan & Parry (2019, 2020*a*) on propeller noise explicitly models the acoustic radiation from steady blade loading and wake interactions as two distinct but coherent sources. They demonstrated that the relative phase between

https://doi.org/10.1017/jfm.2026.11382 Published online by Cambridge University Press

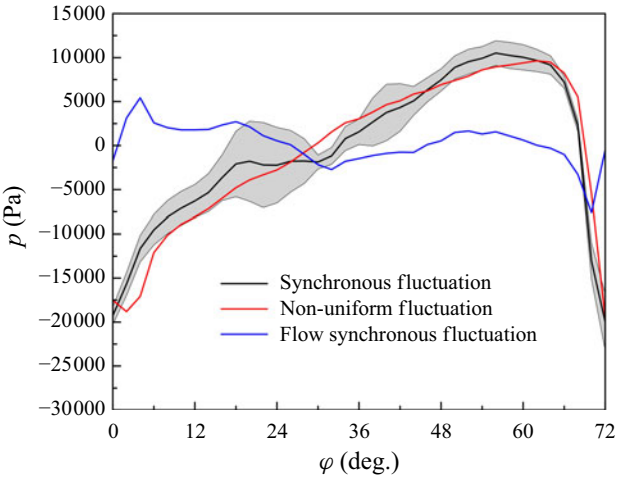


Figure 9. Visualisation of the destructive interference mechanism at point 5. The phase-averaged profiles within a single blade passage (72°) show a local peak in the dynamic p_{FSF} aligning with the primary trough of the dominant kinematic p_{NUF}, resulting in a partial cancellation and a reduced amplitude for the final synchronous signal. The shaded area represents the RMS of the asynchronous fluctuation.

these sources, which can be controlled by geometric parameters such as blade sweep, determines whether the final acoustic signature is amplified or attenuated. The present findings provide a direct fluid-dynamic confirmation of this interference principle at the source, revealing the mechanism that sculpts the pressure field on the shroud wall itself.

Finally, expanding the analysis to the entire shroud surface reveals that this interference pattern is spatially complex. The cross-correlation map in figure 10(*d*) shows that the simple anti-phase relationship observed at point 5 is not universal. Instead, there exist distinct circumferential zones of both destructive (negative correlation) and constructive (positive correlation) interference. This highlights that the intricate spatial pattern of the total synchronous unsteadiness is ultimately sculpted by the spatially varying phase relationship between its powerful kinematic driver and its weaker dynamic modulator.

4. Source-term analysis

4.1. *Governing equations and physical mapping of source components*

To establish a direct causal link between the velocity field dynamics and the observed pressure signatures, the analytical framework turns to the pressure Poisson equation (PPE). While PPE decomposition has been successfully employed in canonical wall-bounded flows to separate ‘rapid’ and ‘slow’ components (Kim 1989; Choi & Moin 1990), its application to the complex, multi-frame interactions of turbomachinery requires a more nuanced approach. In this study, a triple-decomposed PPE framework is formulated to isolate the specific hydrodynamic sources responsible for the kinematic, synchronous and asynchronous pressure fluctuations identified in § 3.

The foundation of the analysis is the instantaneous PPE for an incompressible fluid in a frame of reference rotating at a constant angular velocity $\boldsymbol{\Omega}$. As derived in Appendix A, taking the divergence of the Navier–Stokes equations in the rotating frame yields

$$\nabla^2 P_R = -\rho \nabla \cdot [\nabla \cdot (\boldsymbol{U}_R \boldsymbol{U}_R)] + 2\rho \boldsymbol{\Omega} \cdot (\nabla \times \boldsymbol{U}_R) + 2\rho\, |\boldsymbol{\Omega}|^2, \tag{4.1}$$

https://doi.org/10.1017/jfm.2026.11382 Published online by Cambridge University Press

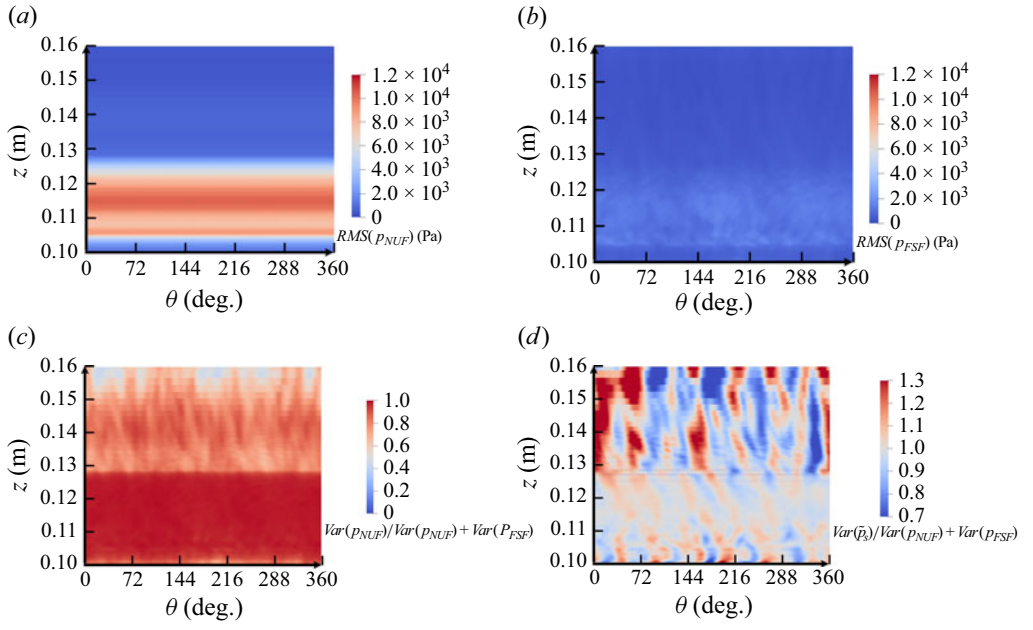


Figure 10. Decomposition of the synchronous fluctuation in the stationary frame. (*a*) The RMS of the non-uniform fluctuation p_{NUF}. (*b*) The RMS of the flow synchronous fluctuation, p_{FSF}. (*c*) Energy fraction of the p_{NUF} component within the synchronous signal. (*d*) Spatial map of the cross-correlation coefficient $C_{NUF,FSF}$ between p_{NUF} and p_{FSF}. This map reveals the complex, spatially varying nature of their interference, with distinct zones of destructive (negative correlation, blue) and constructive (positive correlation, red) interplay.

where $\boldsymbol{U}_R$ is the instantaneous velocity vector in the rotating frame. To dissect the physical origins of each pressure component, the triple decomposition ($\boldsymbol{U}_R = \overline{\boldsymbol{U}}_R + \tilde{\boldsymbol{u}}_R + \boldsymbol{u}'_R$) is applied to (4.1). By leveraging the distinct statistical properties of the time- and phase-averaging operators, the full PPE is partitioned into three independent Poisson equations:

$$\nabla^2 \overline{P}_R = S_{MMF} + S_{SRS} + S_{ARS} + S_{MC} + S_C, \tag{4.2a}$$

$$\nabla^2 \tilde{p}_R = S_{MSI} + S_{SSI} + S_{SMRS} + S_{SC}, \tag{4.2b}$$

$$\nabla^2 p'_R = S_{MAI} + S_{SAI} + S_{ASI} + S_{AC}. \tag{4.2c}$$

The source terms on the right-hand sides of (4.2*a*)–(4.2*c*) represent the negative divergence of specific force densities, providing a rigorous mechanical mapping between flow structures and pressure generation. The detailed mathematical expressions for all thirteen source terms are moved to Appendix B to maintain focus on physical insights. The physical significance of the primary contributors is summarised as follows.

(i) Sources for $\overline{P}_R$ (kinematic p_{NUF}). The dominant term is the mean momentum flux (S_{MMF}), which captures the force gradient established by the steady blade-to-blade loading. The terms S_{SRS} and S_{ARS} represent the steady 'Reynolds forces' exerted by velocity fluctuations on the mean pressure field, while S_{MC} and S_C account for the mean Coriolis and centrifugal force densities.

(ii) Sources for $\tilde{p}_R$ (dynamic p_{FSF}). These terms describe the generation of coherent, tonal unsteadiness: S_{MSI} (mean–synchronous interaction) represents the fluctuating

https://doi.org/10.1017/jfm.2026.11382 Published online by Cambridge University Press

force generated as coherent velocity structures are strained by the mean shear. Notably, S_{SMRS} (synchronous modulation of Reynolds stress) captures the interaction where the large-scale TLV entrains and organises background stochastic turbulence, thereby energising the phase-locked pressure field.

(iii) Sources for p_R' (stochastic p_{FAF}). These terms characterise canonical turbulence processes: S_{ASI} (asynchronous self-interaction) represents the internal forces of the turbulent energy cascade, serving as the pressure-source analogue of momentum transfer across stochastic scales; S_{MAI} characterises the classical turbulence production mechanism via mean shear.

By solving these equations via the Green's function method (as discussed in § 4.2), the relative contribution of each physical mechanism to the total shroud unsteadiness can be quantitatively evaluated.

4.2. *Solution methodology via the Green's function*

The preceding analysis yields a set of PPEs of the general form $\nabla^2 p = S$, each relating a specific pressure component to its corresponding fluid-dynamic sources. The solution to such an elliptic equation can be formally expressed using an integral formulation, providing a direct and physically intuitive link between the source field S and the resulting pressure field p.

For a pressure field $p(\boldsymbol{x}, t)$ within a volume V bounded by a surface ∂V, the exact solution at any observation point $\boldsymbol{x}$ is given by the Kirchhoff–Helmholtz integral

$$p(\boldsymbol{x}, t) = \int_V S(\boldsymbol{x}_0, t)\, G(\boldsymbol{x}, \boldsymbol{x}_0)\, \mathrm{d}V(\boldsymbol{x}_0) + \oint_{\partial V} \left[p(\boldsymbol{x}_0, t) \frac{\partial G}{\partial n}(\boldsymbol{x}, \boldsymbol{x}_0) - G(\boldsymbol{x}, \boldsymbol{x}_0) \frac{\partial p}{\partial n}(\boldsymbol{x}_0, t) \right] \mathrm{d}A(\boldsymbol{x}_0), \tag{4.3}$$

where $\boldsymbol{x}_0$ is the source-point coordinate, n is the outward-pointing normal vector on the boundary, and $G(\boldsymbol{x}, \boldsymbol{x}_0)$ is the domain-specific Green's function that satisfies the appropriate boundary conditions. The volume integral represents the direct contribution from all hydrodynamic sources within the flow, while the surface integral accounts for the influence of the boundaries.

While this formulation is exact, its application to complex internal flows is hindered by the fact that the domain-specific Green's function is generally not known analytically. Therefore, following an established approximation used for source analysis in wall-bounded turbulent flows (Hu, Reiche & Ewert 2017), the pressure field is estimated by considering the volume integral term with the free-space Green's function G_∞:

$$G_\infty(\boldsymbol{x}, \boldsymbol{x}_0) = -\frac{1}{4\pi\, |\boldsymbol{x} - \boldsymbol{x}_0|}. \tag{4.4}$$

The validity of this approximation for the present analysis rests on the characteristic r^{-1} decay of the Green's function, which ensures that the pressure at a given observation point is primarily dictated by the most intense and geographically closest sources. In this incompressible framework, the speed of sound is effectively assumed to be infinite ($c \to \infty$), meaning that pressure disturbances propagate instantaneously, and no time-retardation effect is considered. This assumption is rigorously justified by the operating conditions of the mixed-flow pump; with working fluid water ($c \approx 1480$ m s^{-1}) and impeller tip speed $U_{tip} \approx 13.7$ m s^{-1}, the resulting Mach number is $Ma \approx 0.009$, which is far below the compressibility threshold ($Ma < 0.3$). Consequently, finite wave propagation speeds and compressibility effects are negligible for the hydrodynamic pressure fluctuations investigated here.

https://doi.org/10.1017/jfm.2026.11382 Published online by Cambridge University Press

This approach of using a Green's function integral method to relate local sources to the pressure field has been validated for its accuracy in identifying the mechanistic origins of wall pressure signatures (Wang & Liu 2023). Given that the focus of this study is on the near-field fluctuations on the shroud wall generated by the TLV and blade loading – source mechanisms located in the immediate vicinity of the sensors – this approximation is well-suited to identify the dominant local source regions (You *et al.* 2007; Liu & Tan 2018). Furthermore, the volume integral is particularly insightful for interpreting phase-dependent interactions in turbomachinery. For instance, Suzuki (2023) utilised a similar formulation to quantify the phase interference between rotor wakes and boundary layer instabilities.

Nevertheless, the limitations of using the free-space Green's function in an enclosed pump volute must be acknowledged. This simplification neglects the Kirchhoff–Helmholtz surface integral terms, and fails to account for pressure reflections from the casing or the boundary constraints that enforce the wall-normal pressure gradient ($\partial p/\partial n$). Consequently, while this methodology is a powerful diagnostic tool for source localisation and for disentangling the relative contributions of different mechanisms, it is not intended to predict the absolute pressure magnitude with perfect precision. The primary objective is to identify the spatial origins and the interference patterns that govern the shroud unsteadiness, for which the volume-integral approach provides a direct and physically intuitive mapping.

4.3. *Fluid-dynamic origins of triple sources*

4.3.1. *Non-uniform fluctuation (p_{NUF})*

The fluid-dynamic origins of p_{NUF} are investigated by decomposing the source terms of the time-averaged PPE (4.2*a*) in the rotating frame. As established in § 3, p_{NUF} arises from the kinematic sweep of the steady but azimuthally non-uniform pressure field $\overline{P}_R$. The analysis proceeds in two stages: a global assessment of source magnitudes to identify primary contributors, followed by a nuanced local analysis of their effectiveness in generating azimuthal pressure asymmetry. This dual-stage decomposition is a robust technique for identifying mechanistic contributions in complex internal flows (Cho, Hwang & Choi 2018; Zuo, Memmolo & Pirozzoli 2023).

Figure 11 displays the spatial distributions of the total source and its constituent terms. The mean momentum flux (S_{MMF}, figure 11*b*) emerges as the primary feature, concentrated near the blade surfaces and within the TLV core. Physically, this term encapsulates the influence of mean velocity gradients and is inextricably linked to TLV dynamics. While the formation of the TLV is driven by the global blade loading, the resulting vortex induces a complex three-dimensional flow that, in turn, reshapes the local loading profile. This reciprocal interaction (Marusic *et al.* 2010) renders the S_{MMF} field a direct fluid-dynamic signature of the coupled blade-loading/TLV system. In contrast, the Reynolds stress terms (S_{SRS} and S_{ARS}, figures 11*c,d*) are localised in the high-shear layers surrounding the vortex, while the Coriolis term (S_{MC}, figure 11*e*) exhibits opposite polarities on either side of the TLV, reflecting its counter-rotating nature.

To quantify the global weight of each mechanism, a relative contribution factor F_{S_i} is defined:

$$F_{S_i} = \frac{\int_V |S_i| \, \mathrm{d}V}{\sum_j \int_V |S_j| \, \mathrm{d}V}. \tag{4.5}$$

https://doi.org/10.1017/jfm.2026.11382 Published online by Cambridge University Press

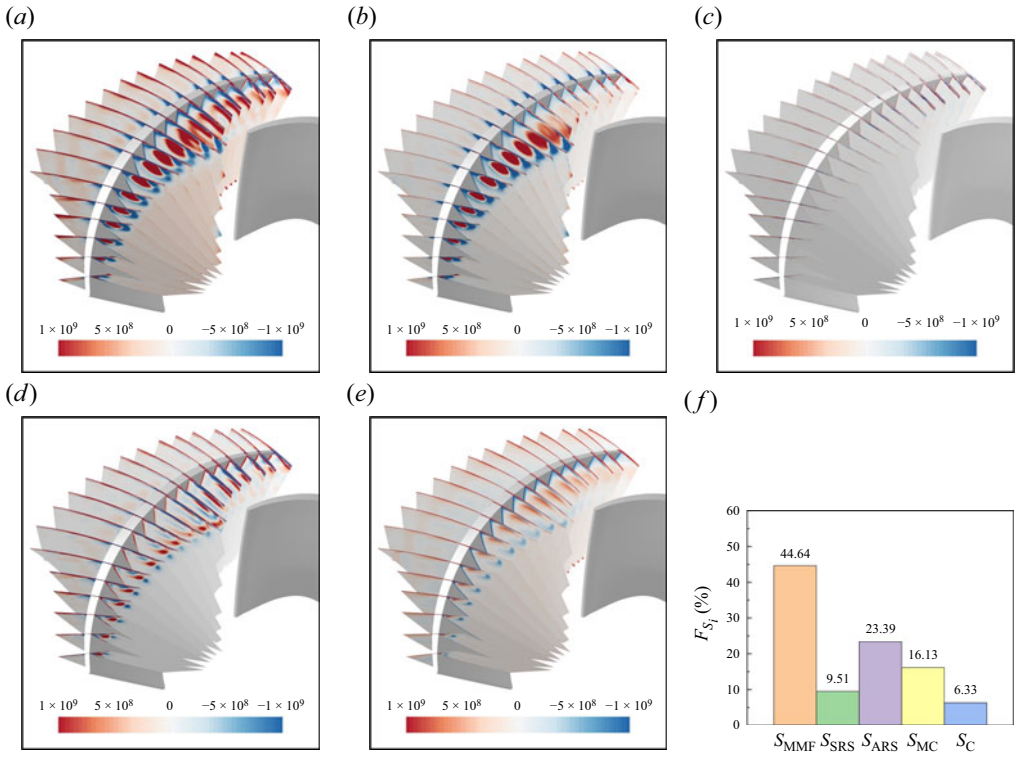


Figure 11. Global analysis of the source terms for the time-averaged pressure field in the rotating frame, $\overline{P}_R$. (*a–e*) Spatial distribution of the source terms within the impeller passages: (*a*) total source $S_R = S_{MMF} + S_{SRS} + S_{ARS} + S_{MC} + S_C$; (*b*) mean momentum flux S_{MMF}; (*c*) synchronous Reynolds stress S_{SRS}; (*d*) asynchronous Reynolds stress S_{ARS}; and (*e*) mean Coriolis effect S_{MC}. The constant centrifugal term S_C is not visualised. (*f*) Fractional contribution of the volume-integrated absolute magnitude of each source term to the global total time-averaged pressure source, as defined by (4.5).

The integration volume V is focused on the impeller domain; sensitivity analysis including the inlet pipe and diffuser confirmed that F_{S_i} values vary by less than 3 % due to the r^{-1} decay of the Green's function, ensuring the spatial robustness of this choice.

Based on this metric, the global analysis (figure 11*f*) reveals a clear hierarchy: S_{MMF} is the principal contributor, accounting for 44.64 % of the total source magnitude, followed by S_{ARS} (23.39 %) and S_{MC} (16.13 %). The minor contributions from S_{SRS} (9.51 %) and the constant centrifugal effect S_C (6.33 %) reinforce the conclusion that blade loading, manifested through the mean momentum flux, is the dominant driver of the stationary pressure footprint.

However, the p_{NUF} perceived by a stationary observer is driven not by the global magnitude of the sources, but by the pressure differential encountered during an azimuthal sweep. A source term's effectiveness in generating this differential is intimately tied to its spatial asymmetry rather than its volume-averaged strength. To precisely quantify how these sources translate into local pressure asymmetry, the Green's function integral (4.3) is utilised.

This local analysis is focused on the representative axial plane at $z^* = 0.67$, situated within the high-intensity fluctuation 'hotspot' (figure 8*a*). The azimuthal pressure difference is defined as $\Delta\overline{P}_R = \overline{P}_R(\boldsymbol{x}_h) - \overline{P}_R(\boldsymbol{x}_l)$, where $\boldsymbol{x}_h$ and $\boldsymbol{x}_l$ denote the locations of maximum and minimum pressure on this plane, respectively. The contribution

https://doi.org/10.1017/jfm.2026.11382 Published online by Cambridge University Press

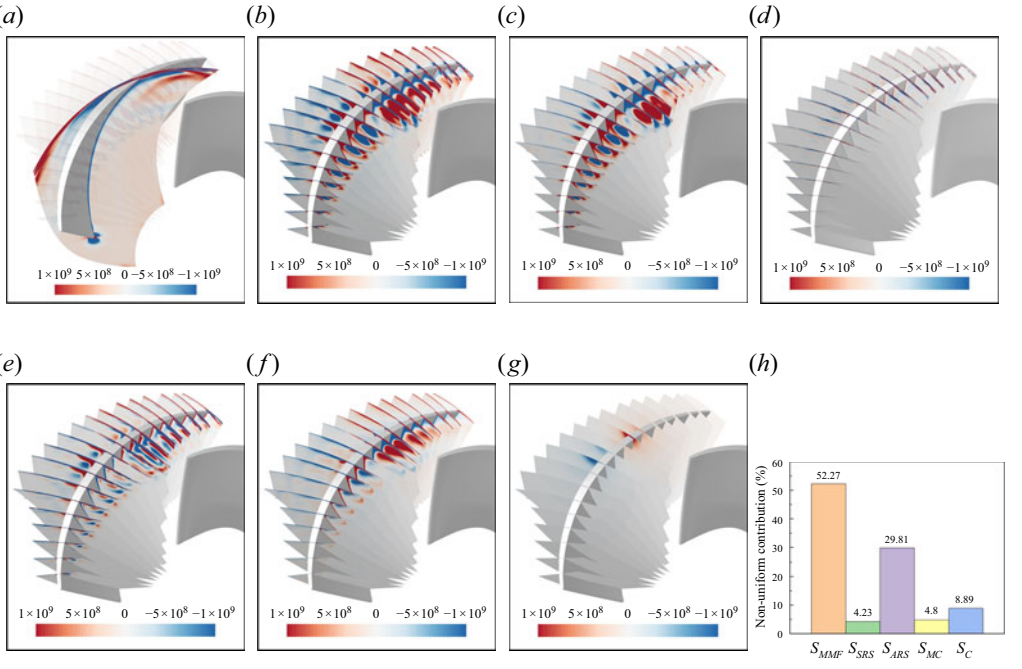


Figure 12. Differential source-term analysis for the azimuthal pressure difference on the representative plane at $z^* = 0.67$. (*a*) Spatial distribution of the total source term S_R on the plane, showing strong positive and negative regions associated with blade loading and tip leakage flow. (*b–g*) Contribution of each source component to the pressure difference. The fields shown are the differential source terms $D_i(\boldsymbol{x}_0) = S_i(\boldsymbol{x}_0)\,[G_\infty(\boldsymbol{x}_h, \boldsymbol{x}_0) - G_\infty(\boldsymbol{x}_l, \boldsymbol{x}_0)]$, which represent the spatially weighted contribution of the source at each point $\boldsymbol{x}_0$ to the total azimuthal pressure difference. The specific terms are: (*b*) total differential source D_R; (*c*) mean momentum flux D_{MMF}; (*d*) synchronous Reynolds stresses D_{SRS}; (*e*) asynchronous Reynolds stresses D_{ARS}; (*f*) mean Coriolis effect D_{MC}; and (*g*) centrifugal effect D_C. (*h*) Fractional contribution of each source term to the total pressure difference, as defined by (4.6).

of each source S_i is evaluated by integrating a differential source term $D_i(\boldsymbol{x}_0) = S_i(\boldsymbol{x}_0)[G_\infty(\boldsymbol{x}_h, \boldsymbol{x}_0) - G_\infty(\boldsymbol{x}_l, \boldsymbol{x}_0)]$ over the flow domain. This term represents the mechanistic attribution of the source at $\boldsymbol{x}_0$ to the overall pressure asymmetry. The fractional contribution factor F_{D_i} is then calculated as

$$F_{D_i} = \frac{\int_V D_i \,\mathrm{d}V}{\sum_j \int_V D_j \,\mathrm{d}V}. \tag{4.6}$$

Figure 12(*a*) illustrates the total source S_R on the selected plane, revealing a highly asymmetric pattern, with strong positive regions near the blade pressure side and intense negative regions associated with the TLV core. The differential source analysis (figures 12*b–h*) provides striking evidence of the dominance of mean momentum flux. As quantified in figure 12(*h*), S_{MMF} is the overwhelming driver of the pressure differential, with its contribution rising to 52.27 %, while S_{ARS} remains significant at 29.81 %.

A comparison between the global (figure 11*f*) and local (figure 12*h*) analyses is illuminating. While S_{MMF} is the dominant source globally (44.64 %), it is even more effective locally (52.27 %), underscoring that its highly asymmetric spatial structure is exceptionally efficient at generating pressure differences. In stark contrast, body forces appear highly inefficient in this context; the contribution of the mean Coriolis effect (S_{MC}) plummets from 16.13 % globally to a negligible 4.8 % locally. This is because

https://doi.org/10.1017/jfm.2026.11382 Published online by Cambridge University Press

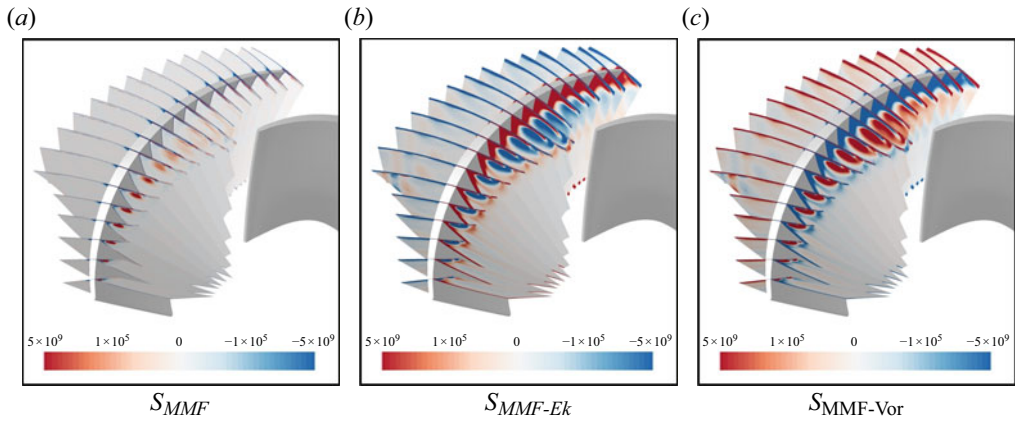


Figure 13. Decomposition of the mean momentum flux source term on multiple axial planes: (*a*) total S_{MMF}; (*b*) kinetic energy source $S_{MMF\text{-}Ek}$; (*c*) vortex interaction source $S_{MMF\text{-}Vor}$. All plots use the same colour scale to highlight the massive spatial cancellation between the dynamic pressure force and the vortex centripetal force.

their spatially smooth and relatively symmetric distributions largely cancel out during the convolution with the differential Green's function. Physically, S_{MMF} is the direct fluid-dynamic manifestation of hydrodynamic blade loading. This establishes a clear causal chain: blade loading dictates the structure of the mean momentum flux field, which, through its inherent spatial asymmetry, serves as the principal generator of the steady pressure non-uniformity perceived as the primary fluctuation in the stationary frame.

To further elucidate the mechanical origins of the dominant p_{NUF} component, the mean momentum flux source (S_{MMF}) is decomposed into two constituent terms representing distinct force-balance mechanisms: a kinetic energy source and a vortex interaction source (the detailed mathematical derivation is provided in Appendix C). The decomposed expression is given by

$$S_{MMF} = \underbrace{-\nabla^2 E_k}_{S_{MMF\text{-}Ek}} + \underbrace{\boldsymbol{\nabla}\cdot(\overline{\boldsymbol{U}}\times\overline{\boldsymbol{\omega}})}_{S_{MMF\text{-}Vor}}, \tag{4.7}$$

where $E_k = (1/2)\,|\overline{\boldsymbol{U}}|^2$ is the mean kinetic energy per unit mass, and $\overline{\boldsymbol{\omega}} = \boldsymbol{\nabla}\times\overline{\boldsymbol{U}}$ is the mean vorticity vector.

Physically, $S_{MMF\text{-}Ek}$ represents the pressure field required to balance the Bernoulli-like dynamic pressure gradient force ($-\boldsymbol{\nabla}E_k$) arising from variations in the mean velocity magnitude. This term is primarily associated with the steady potential-flow field and the global acceleration or deceleration of the bulk fluid as it traverses the impeller. In contrast, $S_{MMF\text{-}Vor}$ represents the divergence of the vortex force (or Lamb vector), capturing the interaction between the mean velocity field and the vorticity distribution. This term provides the direct fluid-dynamic signature of the TLV, and characterises the pressure field induced by the vortex structure as it modifies the mean streamlines. This decomposition establishes a clear causal link between the vortex core dynamics and the observed kinematic pressure sweep.

As visualised in figure 13, the decomposition reveals a striking mechanical phenomenon. Under an identical colour scale, the individual magnitudes of $S_{MMF\text{-}Ek}$ and $S_{MMF\text{-}Vor}$ are found to be an order of magnitude higher than the resultant total source S_{MMF}. Specifically, $S_{MMF\text{-}Ek}$ and $S_{MMF\text{-}Vor}$ exhibit nearly identical spatial distributions but with opposite polarities throughout the blade tip region.

https://doi.org/10.1017/jfm.2026.11382 Published online by Cambridge University Press

This observation confirms that the TLV exists in a state of robust cyclostrophic balance (mechanical equilibrium), where the expansive force arising from dynamic pressure gradients (positive red in figure 13*b*) is almost perfectly counterbalanced by the compressive centripetal force of the Lamb vector (negative blue in figure 13*c*). Crucially, the analysis demonstrates that neither the kinetic energy nor the vortex strength alone dictates the shroud unsteadiness. Instead, the kinematic fluctuation (p_{NUF}) is driven by the residual force imbalance that escapes this internal competition (figure 13*a*). This explains why traditional vortex-identification methods (such as Q-criterion or λ_2), which only capture the morphology of the balanced structure, fail to quantify the specific 'effective leakage' responsible for pressure fluctuations. The three source model thus provides superior diagnostic fidelity by isolating this active residual forcing from the passive, balanced vortex structure.

4.3.2. *Flow synchronous fluctuation (p_{FSF})*

The origins of the flow synchronous fluctuation (p_{FSF}), representing genuine dynamic unsteadiness phase-locked to the rotor, are investigated via the synchronous PPE (4.2*b*). Unlike the kinematic p_{NUF}, the sources of p_{FSF} are Lagrangian-time-dependent, fluctuating at the rotational frequency and its harmonics. In this context, the rotor's rotation acts as an external forcing to which inherent flow instabilities, such as TLV oscillation, become synchronised. This phenomenon is analogous to the control of cylinder wakes, where external excitation locks the natural shedding frequency (Feng & Wang 2010).

Figure 14 presents the spatial distribution and fractional contributions of these source terms, evaluated via the volume-averaged metric (4.5). The total source field (figure 14*a*) is intensely localised along the TLV trajectory, confirming that the vortex region is the primary site for generating phase-locked unsteadiness. The analysis reveals a clear mechanistic hierarchy: the synchronous modulation of Reynolds stress (S_{SMRS}) is overwhelmingly dominant, accounting for 80.22 % of the total source magnitude (figure 14*f*). Spatially, S_{SMRS} (figure 14*d*) is concentrated in the high-shear layers enveloping the TLV core. This term represents the primary pathway by which deterministic vortex dynamics energises the synchronous pressure field: the periodic large-scale motion of the TLV entrains and organises the surrounding smaller-scale turbulence, leading to a phase-locked modulation of the Reynolds stresses. This aligns with the findings of Vela-Martín (2021) on the synchronisation of small-scale vorticity with large-scale dynamics.

The second most significant contributor is the mean–synchronous interaction (S_{MSI}, 16.95 %), which characterises the force fluctuations arising as coherent velocity structures are strained by the mean shear layer (figure 14*b*). This is a canonical mechanism for tonal noise generation in wall-bounded turbulence (Marusic *et al.* 2010). In contrast, the contributions from the nonlinear synchronous self-interaction (S_{SSI}) and the synchronous Coriolis effect (S_{SC}) are negligible. In summary, the dynamic synchronous pressure signatures are principally sculpted by the periodic motion of the TLV, through its dual interaction with background turbulence (S_{SMRS}) and the mean shear field (S_{MSI}).

4.3.3. *Flow asynchronous fluctuation (p_{FAF})*

The broadband, stochastic pressure fluctuations (p_{FAF}) originate from the non-phase-locked velocity interactions in the rotating frame, as described by the asynchronous PPE (4.2*c*). These source terms encompass the non-deterministic spectral energy transfer characteristic of high-Reynolds-number turbulence. As quantified in figure 15, the

https://doi.org/10.1017/jfm.2026.11382 Published online by Cambridge University Press

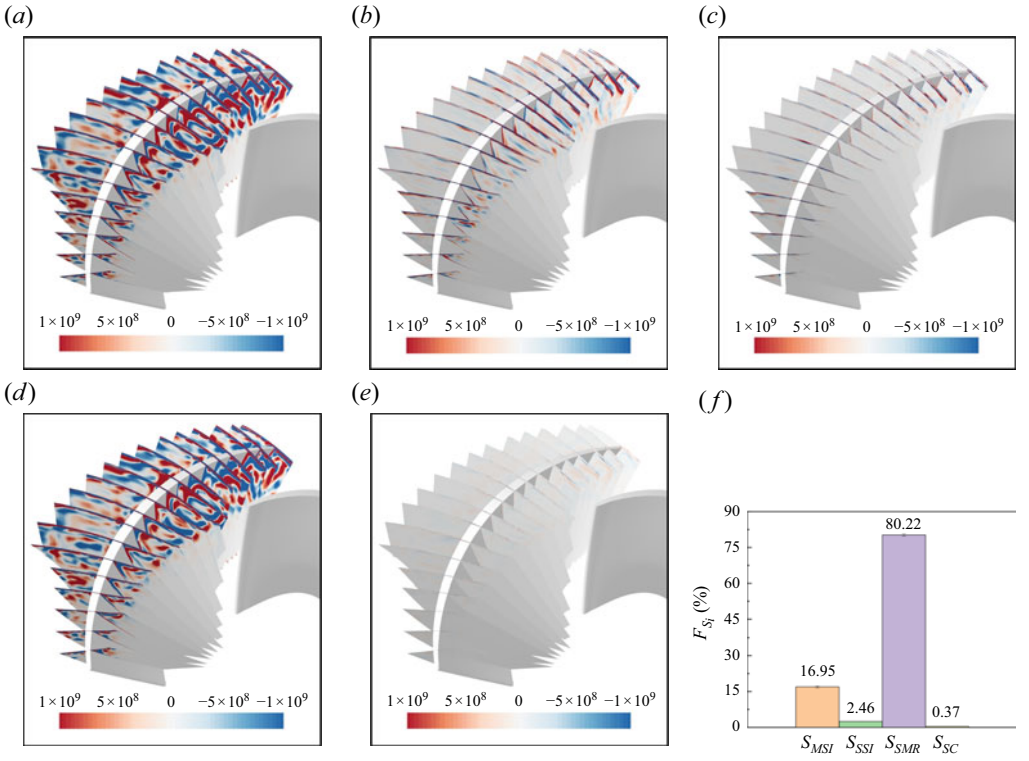


Figure 14. Global analysis of the source terms for the synchronous fluctuation pressure field $\tilde{p}_R$. (*a–e*) Spatial distributions: (*a*) total source $S_{\tilde{p}_R}$; (*b*) mean–synchronous interaction S_{MSI}; (*c*) synchronous self-interaction S_{SSI}; (*d*) synchronous modulation of Reynolds stress S_{SMRS}; (*e*) synchronous Coriolis effect S_{SC}. (*f*) Fractional contributions based on (4.5). Error bars denote the temporal standard deviation.

asynchronous source field is spatially confined to the TLV trajectory and its high-shear periphery, identifying the vortex as the primary nexus for broadband unsteadiness.

The quantitative breakdown (figure 15*f*) reveals that the source field is dominated by two canonical turbulence mechanisms. The principal contributor is the asynchronous self-interaction (S_{ASI}), accounting for 79.33 % of the total magnitude. This term (figure 15*d*) represents the pressure-source analogue of the turbulent energy cascade, formally driven by nonlinear triadic wave interactions that transfer energy across a wide range of stochastic scales (Cho *et al.* 2018). The second significant mechanism is the mean–asynchronous interaction (S_{MAI}, 17.75 %), which characterises the fundamental process of turbulence production (figure 15*b*). Its spatial concentration in the high-shear zones surrounding the TLV confirms that kinetic energy is extracted from the mean flow to energise the incoherent pressure fluctuations in this region (Buaria, Bodenschatz & Pumir 2020).

The contributions from the synchronous–asynchronous interaction (S_{SAI}) and the Coriolis effect (S_{AC}) are negligible. In summary, the broadband pressure signatures on the shroud are primarily sculpted by the dual processes of turbulence production and the subsequent energy cascade, both of which are highly localised and intensified within the unstable shear layers generated by the TLV.

4.4. *Sensitivity to operating conditions and physical robustness*

To evaluate the generalisability and robustness of the triple source model, the source-term analysis is extended across three representative operating conditions: partial load ($0.8Q_d$),

https://doi.org/10.1017/jfm.2026.11382 Published online by Cambridge University Press

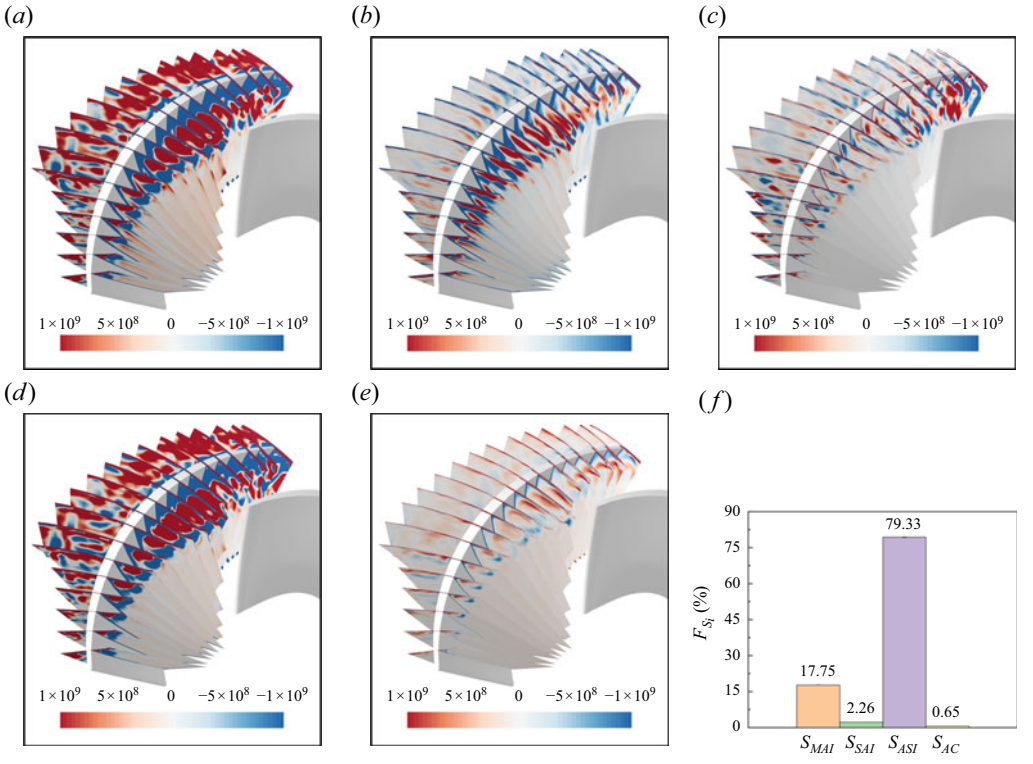


Figure 15. Global analysis of the source terms for the asynchronous fluctuation pressure field p'_R. (*a–e*) Spatial distributions: (*a*) total source $S_{p'_R}$; (*b*) mean–asynchronous interaction S_{MAI}; (*c*) synchronous–asynchronous interaction S_{SAI}; (*d*) asynchronous self-interaction S_{ASI}; (*e*) asynchronous Coriolis effect S_{AC}. (*f*) Time-averaged fractional contributions based on (4.5). Error bars denote the temporal standard deviation.

design point ($1.0Q_d$) and overload ($1.2Q_d$). This analysis serves a dual purpose: first, to assess the model's sensitivity to varying hydraulic loads, and second, to demonstrate that the contribution factors (F_{S_i} and F_{D_i}) are objective physical metrics directly originating from the pump's internal fluid mechanics rather than serving as empirical fitting parameters.

The quantitative results for all three pressure components (p_{NUF}, p_{FSF}, p_{FAF}) and their constituent sources are summarised in table 2. A consistent hierarchy of physical mechanisms is observed across the entire operating range. For the kinematic p_{NUF} component, the mean momentum flux (S_{MMF}) remains the primary driver, contributing between 46.12 % and 52.27 % to the local pressure asymmetry. The synchronous modulation of Reynolds stress (S_{SMRS}) consistently governs the dynamic p_{FSF} component with a dominant share of 75–80 %, while the asynchronous self-interaction (S_{ASI}) remains the principal source for the broadband p_{FAF} fluctuations.

The systematic variations in the contribution factors further highlight the model's diagnostic utility. As the flow rate increases from $0.8Q_d$ to $1.2Q_d$, the relative importance of S_{MMF} for p_{NUF} slightly decreases. This reflects the physical reality that at higher flow rates, the inflow becomes more aligned with the blade geometry, leading to a more uniform momentum flux distribution. Conversely, the centrifugal effect (S_C) exhibits a relative increase in its contribution to pressure asymmetry as loading-related sources weaken. The high degree of consistency in the mechanism hierarchy indicates that the triple source

https://doi.org/10.1017/jfm.2026.11382 Published online by Cambridge University Press

Component	Source mechanism	$0.8Q_d$	$1.0Q_d$	$1.2Q_d$
p_{NUF} (F_{D_i})	S_{MMF} (mean momentum flux)	52.27 %	49.30 %	46.12 %
	S_{ARS} (asynchronous Reynolds stress)	29.81 %	27.50 %	25.10 %
	Others (S_{SRS}, S_{MC}, S_C)	17.92 %	23.20 %	28.78 %
p_{FSF} (F_{S_i})	S_{SMRS} (synchronous modulation of Reynolds stress)	80.22 %	78.50 %	75.30 %
	S_{MSI} (mean–synchronous interaction)	16.95 %	18.20 %	20.10 %
	Others (S_{SSI}, S_{SC})	2.83 %	3.30 %	4.60 %
p_{FAF} (F_{S_i})	S_{ASI} (asynchronous self-interaction)	79.33 %	80.10 %	82.50 %
	S_{MAI} (mean–asynchronous interaction)	17.75 %	16.50 %	14.20 %
	Others (S_{SAI}, S_{AC})	2.92 %	3.40 %	3.30 %

Table 2. Comparison of the contribution factors for p_{NUF}, p_{FSF} and p_{FAF} across different operating conditions.

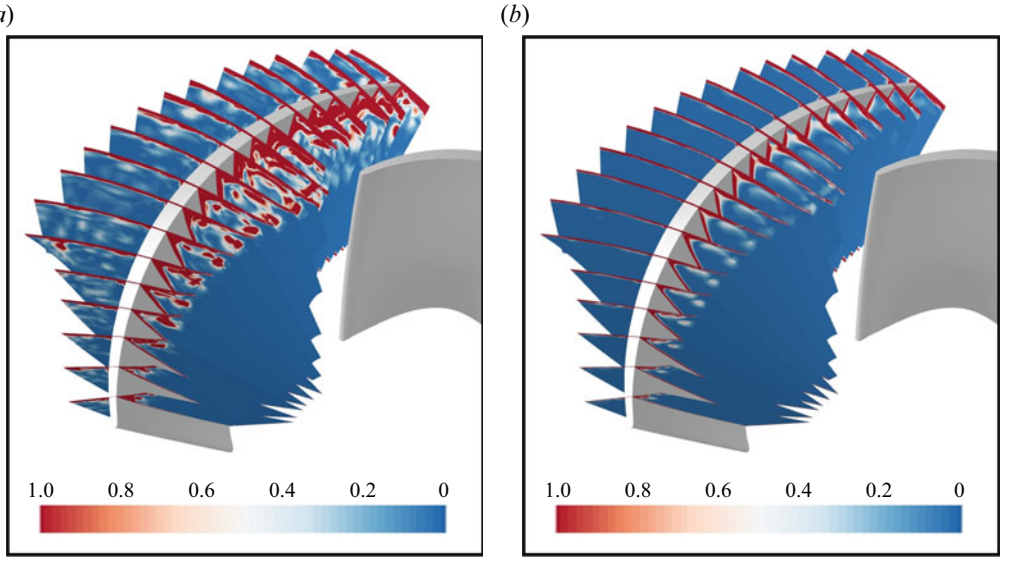


Figure 16. Spatial distribution of the NIP between source components: (*a*) NIP between p_{NUF} and p_{FSF} sources; (*b*) NIP between p_{NUF} and p_{FAF} sources. The scale identifies hotspots of physical coupling, highlighting the TLV as the common physical nexus for all components.

model captures the fundamental, invariant features of turbomachinery unsteadiness while remaining responsive to changes in the operating state.

To address the underlying physical connection between the decomposed sources, a spatial correlation analysis based on the normalised intensity product (NIP) is performed. The NIP is defined as the product of the local source magnitudes normalised by their respective spatial means:

$$NIP_{A,B}(\boldsymbol{x}) = \frac{|S_A(\boldsymbol{x})|}{\langle |S_A| \rangle} \times \frac{|S_B(\boldsymbol{x})|}{\langle |S_B| \rangle}. \tag{4.8}$$

This metric identifies hotspots where different mechanisms simultaneously exert high-intensity forcing on the pressure field.

Figure 16 displays the NIP maps between the kinematic source (p_{NUF}) and the two dynamic sources (p_{FSF} and p_{FAF}). A striking spatial co-location is observed: the coupling hotspots are strictly localised along the trajectory of the TLV and within the high-shear

https://doi.org/10.1017/jfm.2026.11382 Published online by Cambridge University Press

layers near the shroud. Physically, these results demonstrate that although the triple source model mathematically partitions the signal, these components share a common physical nexus. The TLV acts as the primary engine that simultaneously generates the steady pressure footprint (p_{NUF}), triggers the phase-locked dynamic modulations (p_{FSF}), and energises the stochastic fluctuations (p_{FAF}). The near-perfect spatial congruence at the vortex core confirms that the observed shroud unsteadiness is a multifaceted manifestation of the same underlying vortex dynamics, justifying the use of the triple source model to diagnose the distinct impacts of a single coherent structure.

5. Conclusions

This work presents a comprehensive investigation into the physical origins of pressure fluctuations on the stationary shroud wall of a mixed-flow pump. The integration of high-fidelity stress-blended eddy simulation with a novel triple source model successfully disentangles the convoluted contributions to wall unsteadiness. The triple source model partitions the signal into three physically interpretable components: (i) the kinematic non-uniform fluctuation (p_{NUF}) originating from the steady loading sweep; (ii) the dynamic flow synchronous fluctuation (p_{FSF}) representing phase-locked instabilities; and (iii) the stochastic flow asynchronous fluctuation (p_{FAF}) arising from the turbulent cascade. By coupling this decomposition with a source-term analysis of the pressure Poisson equation (PPE), each component was traced back to specific fluid-dynamic interactions in the rotating frame.

The first key conclusion is that the shroud pressure field is overwhelmingly dominated by deterministic, synchronous fluctuations, which account for over 90 % of the total fluctuation energy in the high-intensity regions. The triple source model reveals that this unsteadiness is not monolithic but results from a complex interplay between the powerful kinematic p_{NUF} and the subtler dynamic p_{FSF}. A crucial insight is the discovery of destructive interference between these components. At the blade tip, the dynamic oscillation of the leakage vortex is found to be largely out of phase with the deep pressure trough of the mean vortex field, effectively dampening the final observed synchronous signal. This finding establishes that the perceived wall unsteadiness is a delicate superposition of a kinematic driver and its dynamic modulator, rather than a single physical event.

Second, the PPE source-term analysis identifies the mean momentum flux (S_{MMF}) as the primary root cause of p_{NUF}, contributing 52.27 % to the local pressure asymmetry. This term is a direct manifestation of the hydrodynamic blade loading and its interaction with the TLV. Local analysis demonstrates that the r^{-1} decay and the high spatial asymmetry of S_{MMF} make it exceptionally efficient at generating pressure differentials. In contrast, body forces such as the Coriolis effect are locally inefficient due to significant spatial cancellation. This establishes a clear causal chain from the chordwise blade loading distribution to the principal component of the observed wall pressure fluctuations.

Finally, the study elucidates the origins of the genuine dynamic unsteadiness. The phase-locked p_{FSF} is primarily driven by the synchronous modulation of Reynolds stress (S_{SMRS}), accounting for 80.22 % of its source magnitude. This identifies the interaction between the periodic motion of the TLV and the background turbulence as the dominant dynamic mechanism. Meanwhile, the broadband p_{FAF} is sourced from the asynchronous self-interaction (S_{ASI}), which characterises the turbulent energy cascade. All dynamic source mechanisms are intensely localised within the unsteady shear layers of the TLV, confirming the vortex core as the central physical nexus governing the multifaceted impact of turbomachinery unsteadiness.

https://doi.org/10.1017/jfm.2026.11382 Published online by Cambridge University Press

Beyond these physical insights, this work establishes a systematic four-level design methodology for developing low-noise and low-vibration turbomachinery. At the macro level, the triple source model provides strategic direction by distinguishing whether shroud unsteadiness is a geometric footprint issue (p_{NUF}) or a flow instability issue (p_{FSF}), ensuring the correct selection of suppression strategies. At the second level, the discovery of phase-interaction engineering enables cancellation by design. By modulating the phase relationship between the kinematic and dynamic components through parameters such as blade sweep or lean, designers can achieve amplitude reduction via anti-phase cancellation. At the third level, the source-term analysis provides a deep mechanistic diagnosis that pinpoints the fluid-dynamic genes of the fluctuations, e.g. shifts from treating the pressure signal as a black box to targeting the mean momentum flux asymmetry. Finally, this framework facilitates active design by establishing a direct causal mapping between dominant sources and geometric implementation, such as modifying chordwise loading to homogenise momentum flux, or utilising casing treatments to stabilise vortex dynamics.

While this study acknowledges limitations such as the under-prediction of high-frequency turbulence in hybrid RANS–LES and the use of an approximate Green's function, the proposed diagnostic framework moves beyond simple post-processing to provide a rigorous physical basis for targeted mitigation. These insights will be instrumental in accelerating the design and optimisation cycles for the next generation of quieter, more stable mixed-flow pumps.

Acknowledgements. This work was supported by the National Key Research and Development Programme of China (2024YFB3410003).

Declaration of interests. The authors report no conflict of interest.

Appendix A. Derivation of the PPE in a rotating frame

The derivation begins with the incompressible Navier–Stokes momentum equation in a frame of reference rotating with a constant angular velocity $\boldsymbol{\Omega}$:

$$\frac{\partial \boldsymbol{u}_R}{\partial t} + (\boldsymbol{u}_R \cdot \boldsymbol{\nabla})\boldsymbol{u}_R + 2\boldsymbol{\Omega} \times \boldsymbol{u}_R + \boldsymbol{\Omega} \times (\boldsymbol{\Omega} \times \boldsymbol{r}) = -\frac{1}{\rho}\boldsymbol{\nabla} P + \nu\, \nabla^2 \boldsymbol{u}_R, \tag{A1}$$

where $\boldsymbol{u}_R$ is the velocity vector in the rotating frame, P is the static pressure, ρ is the fluid density, ν is the kinematic viscosity, and $\boldsymbol{r}$ is the position vector. The terms on the left-hand side represent the local acceleration, convective acceleration, Coriolis acceleration and centrifugal acceleration, respectively.

To obtain the equation for pressure, we take the divergence ($\boldsymbol{\nabla}\cdot$) of (A1). For an incompressible fluid, the continuity equation requires $\boldsymbol{\nabla} \cdot \boldsymbol{u}_R = 0$. Consequently, the divergence of the unsteady term vanishes:

$$\boldsymbol{\nabla} \cdot \frac{\partial \boldsymbol{u}_R}{\partial t} = \frac{\partial}{\partial t}(\boldsymbol{\nabla} \cdot \boldsymbol{u}_R) = 0. \tag{A2}$$

Similarly, the divergence of the viscous term vanishes for a solenoidal velocity field:

$$\boldsymbol{\nabla} \cdot (\nu\, \nabla^2 \boldsymbol{u}_R) = \nu\, \nabla^2 (\boldsymbol{\nabla} \cdot \boldsymbol{u}_R) = 0. \tag{A3}$$

Now we analyse the divergence of the remaining terms.

(i) Pressure term:

$$\boldsymbol{\nabla} \cdot \left(-\frac{1}{\rho}\boldsymbol{\nabla} P \right) = -\frac{1}{\rho}\nabla^2 P. \tag{A4}$$

https://doi.org/10.1017/jfm.2026.11382 Published online by Cambridge University Press

(ii) Convective term: using the tensor identity $\nabla \cdot [(\boldsymbol{u} \cdot \nabla)\boldsymbol{u}] = \nabla \cdot [\nabla \cdot (\boldsymbol{u}\boldsymbol{u})]$, this becomes

$$\nabla \cdot [(\boldsymbol{u}_R \cdot \nabla)\boldsymbol{u}_R] = \nabla \cdot [\nabla \cdot (\boldsymbol{u}_R\boldsymbol{u}_R)]. \tag{A5}$$

(iii) Coriolis term: using the vector identity $\nabla \cdot (\boldsymbol{A} \times \boldsymbol{B}) = \boldsymbol{B} \cdot (\nabla \times \boldsymbol{A}) - \boldsymbol{A} \cdot (\nabla \times \boldsymbol{B})$, and noting that $\boldsymbol{\Omega}$ is constant ($\nabla \times \boldsymbol{\Omega} = 0$), gives

$$\nabla \cdot (2\boldsymbol{\Omega} \times \boldsymbol{u}_R) = -2\boldsymbol{\Omega} \cdot (\nabla \times \boldsymbol{u}_R). \tag{A6}$$

(iv) Centrifugal term: the centrifugal force can be written as the gradient of a potential, $\boldsymbol{\Omega} \times (\boldsymbol{\Omega} \times \boldsymbol{r}) = -\nabla((1/2)|\boldsymbol{\Omega} \times \boldsymbol{r}|^2)$. Direct evaluation of the divergence yields

$$\nabla \cdot [\boldsymbol{\Omega} \times (\boldsymbol{\Omega} \times \boldsymbol{r})] = -2\,|\boldsymbol{\Omega}|^2. \tag{A7}$$

Rearranging the terms to isolate the pressure Laplacian on the left-hand side yields the PPE in the rotating frame:

$$\nabla^2 P = -\rho \nabla \cdot [\nabla \cdot (\boldsymbol{u}_R\boldsymbol{u}_R)] + 2\rho\boldsymbol{\Omega} \cdot (\nabla \times \boldsymbol{u}_R) + 2\rho\,|\boldsymbol{\Omega}|^2. \tag{A8}$$

This matches (4.1) presented in the main text, where the source term S now incorporates the fluid density ρ.

Appendix B. Mathematical expressions of the PPE source terms

The source terms of the triple-decomposed PPE, as presented in (4.2*a*)–(4.2*c*), are explicitly defined as follows.

(i) Sources for the time-averaged field $\overline{P}_R$:

$$S_{MMF} = -\rho \nabla \cdot [\nabla \cdot (\overline{\boldsymbol{U}}_R\overline{\boldsymbol{U}}_R)], \tag{B1a}$$

$$S_{SRS} = -\rho \nabla \cdot [\nabla \cdot (\overline{\tilde{\boldsymbol{u}}_R\tilde{\boldsymbol{u}}_R})], \tag{B1b}$$

$$S_{ARS} = -\rho \nabla \cdot [\nabla \cdot (\overline{\boldsymbol{u}'_R\boldsymbol{u}'_R})], \tag{B1c}$$

$$S_{MC} = 2\rho\boldsymbol{\Omega} \cdot (\nabla \times \overline{\boldsymbol{U}}_R), \tag{B1d}$$

$$S_C = 2\rho\,|\boldsymbol{\Omega}|^2. \tag{B1e}$$

(ii) Sources for the synchronous fluctuation $\tilde{p}_R$:

$$S_{MSI} = -\rho \nabla \cdot [\nabla \cdot (\overline{\boldsymbol{U}}_R\tilde{\boldsymbol{u}}_R + \tilde{\boldsymbol{u}}_R\overline{\boldsymbol{U}}_R)], \tag{B2a}$$

$$S_{SSI} = -\rho \nabla \cdot [\nabla \cdot (\tilde{\boldsymbol{u}}_R\tilde{\boldsymbol{u}}_R - \overline{\tilde{\boldsymbol{u}}_R\tilde{\boldsymbol{u}}_R})], \tag{B2b}$$

$$S_{SMRS} = -\rho \nabla \cdot [\nabla \cdot (\langle \boldsymbol{u}'_R\boldsymbol{u}'_R \rangle_R - \overline{\boldsymbol{u}'_R\boldsymbol{u}'_R})], \tag{B2c}$$

$$S_{SC} = 2\rho\boldsymbol{\Omega} \cdot (\nabla \times \tilde{\boldsymbol{u}}_R). \tag{B2d}$$

(iii) Sources for the asynchronous fluctuation p'_R:

$$S_{MAI} = -\rho \nabla \cdot [\nabla \cdot (\overline{\boldsymbol{U}}_R\boldsymbol{u}'_R + \boldsymbol{u}'_R\overline{\boldsymbol{U}}_R)], \tag{B3a}$$

$$S_{SAI} = -\rho \nabla \cdot [\nabla \cdot (\tilde{\boldsymbol{u}}_R\boldsymbol{u}'_R + \boldsymbol{u}'_R\tilde{\boldsymbol{u}}_R - \langle \tilde{\boldsymbol{u}}_R\boldsymbol{u}'_R + \boldsymbol{u}'_R\tilde{\boldsymbol{u}}_R \rangle_R)], \tag{B3b}$$

$$S_{ASI} = -\rho \nabla \cdot [\nabla \cdot (\boldsymbol{u}'_R\boldsymbol{u}'_R - \langle \boldsymbol{u}'_R\boldsymbol{u}'_R \rangle_R)], \tag{B3c}$$

$$S_{AC} = 2\rho\boldsymbol{\Omega} \cdot (\nabla \times \boldsymbol{u}'_R). \tag{B3d}$$

https://doi.org/10.1017/jfm.2026.11382 Published online by Cambridge University Press

Appendix C. Decomposition of the mean momentum flux source

The mean momentum flux source term S_{MMF} is defined as the negative divergence of the mean convective acceleration multiplied by the constant density ρ. For an incompressible flow where the continuity equation $\nabla \cdot \overline{\boldsymbol{U}} = 0$ holds, the derivation proceeds as follows.

First, we express S_{MMF} in terms of the convective acceleration:

$$S_{MMF} = -\rho \nabla \cdot [\nabla \cdot (\overline{\boldsymbol{U}}\,\overline{\boldsymbol{U}})] = -\rho \nabla \cdot [(\overline{\boldsymbol{U}} \cdot \nabla)\overline{\boldsymbol{U}}]. \tag{C1}$$

Using the standard vector identity for the convective acceleration:

$$(\overline{\boldsymbol{U}} \cdot \nabla)\overline{\boldsymbol{U}} = \nabla \left(\frac{1}{2} |\overline{\boldsymbol{U}}|^2 \right) - \overline{\boldsymbol{U}} \times (\nabla \times \overline{\boldsymbol{U}}). \tag{C2}$$

Defining the mean kinetic energy per unit mass as $E_k = (1/2)\,|\overline{\boldsymbol{U}}|^2$ and the mean vorticity vector as $\overline{\boldsymbol{\omega}} = \nabla \times \overline{\boldsymbol{U}}$, the source term can be expanded as

$$\begin{aligned} S_{MMF} &= -\rho \nabla \cdot [\nabla E_k - (\overline{\boldsymbol{U}} \times \overline{\boldsymbol{\omega}})] \\ &= -\rho \nabla \cdot (\nabla E_k) + \rho \nabla \cdot (\overline{\boldsymbol{U}} \times \overline{\boldsymbol{\omega}}) \\ &= -\rho\, \nabla^2 E_k + \rho \nabla \cdot (\overline{\boldsymbol{U}} \times \overline{\boldsymbol{\omega}}). \end{aligned} \tag{C3}$$

This result partitions the total S_{MMF} into two mechanical components: a kinetic energy source ($-\rho\, \nabla^2 E_k$) and a vortex interaction source ($\rho \nabla \cdot (\overline{\boldsymbol{U}} \times \overline{\boldsymbol{\omega}})$).

References

Adamczyk, J.J. 1999 Aerodynamic analysis of multistage turbomachinery flows in support of aerodynamic design. *J. Turbomachin.* **122** (2), 189–217.

Buaria, D., Bodenschatz, E. & Pumir, A. 2020 Vortex stretching and enstrophy production in high Reynolds number turbulence. *Phys. Rev. Fluids* **5** (10), 104602.

Callenaere, M., Franc, J.-P., Michel, J.-M. & Riondet, M. 2001 The cavitation instability induced by the development of a re-entrant jet. *J. Fluid Mech.* **444**, 223–256.

Camussi, R., Grilliat, J., Caputi-Gennaro, G. & Jacob, M.C. 2010 Experimental study of a tip leakage flow: wavelet analysis of pressure fluctuations. *J. Fluid Mech.* **660**, 87–113.

Cho, M., Hwang, Y. & Choi, H. 2018 Scale interactions and spectral energy transfer in turbulent channel flow. *J. Fluid Mech.* **854**, 474–504.

Choi, H. & Moin, P. 1990 On the space–time characteristics of wall-pressure fluctuations. *Phys. Fluids A: Fluid Dyn.* **2** (8), 1450–1460.

Duan, X., Jing, J., Zhang, X., Cheng, J. & Li, J. 2024 Broadband pressure spectra induced by unsteady flow in axial turbine. *Intl J. Mech. Sci.* **281**, 109576.

Feng, J., Benra, F.K. & Dohmen, H.J. 2007 Qualitative comparison between numerical and experimental results of unsteady flow in a radial diffuser pump. *J. Vis.* **10** (4), 349–357.

Feng, L.H. & Wang, J.J. 2010 Circular cylinder vortex-synchronization control with a synthetic jet positioned at the rear stagnation point. *J. Fluid Mech.* **662**, 232–259.

Fröhlich, J. & von Terzi, D. 2008 Hybrid LES/RANS methods for the simulation of turbulent flows. *Prog. Aerosp. Sci.* **44** (5), 349–377.

Hall, K. & Clark, W. 1991 Prediction of unsteady aerodynamic loads in cascades using the linearized Euler equations on deforming grids. In *27th Joint Propulsion Conference*. American Institute of Aeronautics and Astronautics.

Han, B., Tan, L. & Han, Y. 2024 Role of wall roughness on interaction of leakage flow and main flow in a mixed flow pump with tip clearance. *Phys. Fluids* **36** (1), 015121.

Han, Y. & Tan, L. 2023*a* Experimental investigation on spatial–temporal evolution of tip leakage cavitation in a mixed flow pump with tip clearance. *Intl J. Multiphase Flow* **164**, 104445.

Han, Y. & Tan, L. 2023*b* Spatial–temporal evolution of tip leakage cavitation with double-hump in a mixed flow pump with tip clearance. *Phys. Fluids* **35** (4), 045152.

Hu, N. 2022 Sensor-size-related attenuation correction of wall pressure spectra measurements. *Phys. Fluids* **34** (6), 067119.

https://doi.org/10.1017/jfm.2026.11382 Published online by Cambridge University Press

HU, N., REICHE, N. & EWERT, R. 2017 Simulation of turbulent boundary layer wall pressure fluctuations via Poisson equation and synthetic turbulence. *J. Fluid Mech.* **826**, 421–454.
HUANG, J., DUAN, L., CASPER, K.M., WAGNILD, R.M. & BITTER, N.P. 2024 Transducer resolution effect on pressure fluctuations beneath hypersonic turbulent boundary layers. *AIAA J.* **62** (3), 882–895.
KAMEIER, F. & NEISE, W. 1997 Rotating blade flow instability as a source of noise in axial turbomachines. *J. Sound Vib.* **203** (5), 833–853.
KELLER, J., KUMAR, P. & MAHESH, K. 2018 Examination of propeller sound production using large eddy simulation. *Phys. Rev. Fluids* **3** (6), 064601.
KEMP, N.H. & SEARS, W.R. 1953 Aerodynamic interference between moving blade rows. *J. Aeronaut. Sci.* **20** (9), 585–597.
KIM, J. 1989 On the structure of pressure fluctuations in simulated turbulent channel flow. *J. Fluid Mech.* **205**, 421–451.
KINGAN, M.J. & PARRY, A.B. 2019 Acoustic theory of the many-bladed contra-rotating propeller: analysis of the effects of blade sweep on wake interaction noise. *J. Fluid Mech.* **868**, 385–427.
KINGAN, M.J. & PARRY, A.B. 2020*a* Acoustic theory of the many-bladed contra-rotating propeller: the effects of sweep on noise enhancement and reduction. *J. Sound Vib.* **468**, 115089.
KINGAN, M.J. & PARRY, A.B. 2020*b* Time-domain analysis of contra-rotating propeller noise: wake interaction with a downstream propeller blade. *J. Fluid Mech.* **901**, A21.
LI, F., HUANG, Q., SUN, G., PAN, G., LI, H. & BAI, C. 2023 Numerical simulation of the flow field and radiation noise from a pump-jet propulsor under various stator pre-whirl angles. *Appl. Ocean Res.* **135**, 103558.
LI, H., WANG, J., ZHANG, J., ZHANG, Z. & HUA, H. 2024 Study on rotor–stator interaction in a pump-jet propulsor based on dynamic mode decomposition. *Phys. Fluids* **36** (4), 045130.
LIANG, A., LI, H., ZHANG, W., YAO, Z., ZHU, B. & WANG, F. 2024 Study on pressure fluctuation and rotating stall characteristics in the vaneless space of a pump-turbine in pump mode. *J. Energy Storage* **94**, 112385.
LIGNAROLO, L.E.M., RAGNI, D., SCARANO, F., SIMÃO FERREIRA, C.J. & VAN BUSSEL, G.J.W. 2015 Tip-vortex instability and turbulent mixing in wind-turbine wakes. *J. Fluid Mech.* **781**, 467–493.
LIU, Y. & TAN, L. 2018 Tip clearance on pressure fluctuation intensity and vortex characteristic of a mixed flow pump as turbine at pump mode. *Renew. Energy* **129**, 606–615.
LU, Y., TAN, L., HAN, Y. & LIU, M. 2022 Cavitation–vibration correlation of a mixed flow pump under steady state and fast start-up conditions by experiment. *Ocean Engng* **251**, 111158.
LUO, X.-Q., GE, Z.-G., FENG, J.-J., ZHU, G.-J., LI, C.-H. & HE, D.-H. 2024 Experimental investigation of pressure fluctuation in a mixed-flow pump under gas–liquid two-phase flow conditions. *Phys. Fluids* **36** (2), 023361.
LV, H., GUO, L., ZHAO, K., DAI, J., LI, Y. & CHEN, S. 2024 Insight into blade tip vibration and deformation characteristics of boiler circulation pumps induced by tip leakage vortex under different tip clearances. *Phys. Fluids* **36** (4), 045114.
MAO, Y., GU, X., XU, C. & YANG, D. 2024 Triple decomposition of unsteady flow in a low-speed mixed-flow fan. *AIAA J.* **62** (1), 302–325.
MAO, Y., GU, X., XU, C. & ZHOU, L. 2025 Identification of aeroacoustic dipole sources of subsonic fan with active acoustic intensity method. *Mech. Syst. Signal Process.* **227**, 112391.
MARUSIC, I., MCKEON, B.J., MONKEWITZ, P.A., NAGIB, H.M., SMITS, A.J. & SREENIVASAN, K.R. 2010 Wall-bounded turbulent flows at high Reynolds numbers: recent advances and key issues. *Phys. Fluids* **22** (6), 065103.
MENTER, F.R. 1994 Two-equation eddy-viscosity turbulence models for engineering applications. *AIAA J.* **32** (8), 1598–1605.
MENTER, F.R. & EGOROV, Y. 2010 The scale-adaptive simulation method for unsteady turbulent flow predictions. Part 1: theory and model description. *Flow Turbul. Combust.* **85** (1), 113–138.
PARRY, A.B. & CRIGHTON, D. 1989 Prediction of counter-rotation propeller noise. In *12th Aeroacoustic Conference*. American Institute of Aeronautics and Astronautics.
PARRY, A.B. 1995 The effect of blade sweep on the reduction and enhancement of supersonic propeller noise. *J. Fluid Mech.* **293**, 181–206.
PARRY, A.B. & KINGAN, M.J. 2019 Acoustic theory of the many-bladed contra-rotating propeller: physics of the wake interaction noise critical sources. *J. Fluid Mech.* **880**, R1.
PARRY, A.B. & KINGAN, M.J. 2021 Acoustic theory of the many-bladed contra-rotating propeller: the event line and the precession of the interaction source. *J. Fluid Mech.* **909**, R1.
QUAGLIA, M.E., LÉONARD, T., MOREAU, S. & ROGER, M. 2017 A 3D analytical model for orthogonal blade–vortex interaction noise. *J. Sound Vib.* **399**, 104–123.

https://doi.org/10.1017/jfm.2026.11382 Published online by Cambridge University Press

REYNOLDS, W.C. & HUSSAIN, A.K.M.F. 1972 The mechanics of an organized wave in turbulent shear flow. Part 3. Theoretical models and comparisons with experiments. *J. Fluid Mech.* **54** (2), 263–288.

ROGER, M., SCHRAM, C. & MOREAU, S. 2014 On vortex–airfoil interaction noise including span-end effects, with application to open-rotor aeroacoustics. *J. Sound Vib.* **333** (1), 283–306.

SHI, S., TANG, W. & HUANG, X. 2022 Wake flow characteristics and unsteady performance of a pump-jet propulsor under hull condition. *Phys. Fluids* **34** (12), 127110.

SUN, W. & TAN, L. 2020 Cavitation–vortex–pressure fluctuation interaction in a centrifugal pump using bubble rotation modified cavitation model under partial load. *J. Fluids Engng* **142** (5), 051206.

SUZUKI, T. 2023 Spiral flow instability between a rotor and a stator in high-speed turbomachinery and its relation to fan noise. *J. Fluid Mech.* **966**, A1.

TYLER, J.M. & SOFRIN, T.G. 1962 Axial flow compressor noise studies. *SAE Trans.* **70**, 309–332.

VELA-MARTÍN, A. 2021 The synchronisation of intense vorticity in isotropic turbulence. *J. Fluid Mech.* **913**, R8.

VIRGILIO, M., BILER, H., CHAITANYA, P. & GANAPATHISUBRAMANI, B. 2024 Observations on the structure of turbulent boundary layers interacting with embedded propeller tip vortices. *J. Fluid Mech.* **1000**, A81.

WANG, Q. & LIU, X. 2023 Green's function integral method for pressure reconstruction from measured pressure gradient and the interpretation of omnidirectional integration. *Phys. Fluids* **35** (7), 077113.

WEI, Z., LI, X., TAO, R., SUN, D., XIAO, R. & HU, H. 2025 Clocking effect of relative position matching on the hydrodynamic and flow-induced noise characteristics in a centrifugal pump. *Appl. Acoust.* **240**, 110899.

WIDMER, C., STAUBLI, T. & LEDERGERBER, N. 2011 Unstable characteristics and rotating stall in turbine brake operation of pump-turbines. *J. Fluids Engng* **133** (4), 041101.

YANG, F., CHANG, P., HU, W., MAO, B., LIU, C. & LI, Z. 2021 Numerical study on pressure pulsation in a slanted axial-flow pump device under partial loads. *Processes* **9** (8), 1404.

YOU, D., WANG, M., MOIN, P. & MITTAL, R. 2007 Large-eddy simulation analysis of mechanisms for viscous losses in a turbomachinery tip-clearance flow. *J. Fluid Mech.* **586**, 177–204.

ZHANG, N., DONG, H., ZHENG, F., GAD, M., LI, D. & GAO, B. 2025 Investigation of the impact of rotor–stator matching modes on the pressure pulsations of the guide vane centrifugal pump. *Ann. Nucl. Energy* **214**, 111189.

ZUO, F.-Y., MEMMOLO, A. & PIROZZOLI, S. 2023 On wall pressure fluctuations in conical shock wave/turbulent boundary layer interaction. *J. Fluid Mech.* **967**, A3.

ZUO, Z., LIU, S., SUN, Y. & WU, Y. 2015 Pressure fluctuations in the vaneless space of high-head pump-turbines – a review. *Renew. Sustain. Energy Rev.* **41**, 965–974.

https://doi.org/10.1017/jfm.2026.11382 Published online by Cambridge University Press